International Journal of Heat and Fluid Flow 117 (2026) 110126

Contents lists available at ScienceDirect

International Journal of Heat and Fluid Flow

journal homepage: www.elsevier.com/locate/ijhff

# Roughness effects on turbulent flows over Gaussian geometries using Large Eddy Simulations

Federica Bruno [a],*, Enrico Napoli [b], Mauro De Marchis [b]

[a] Dipartimento di Ingegneria e Architettura, Università degli Studi di Enna Kore, Italy
[b] Dipartimento di Ingegneria, Università degli Studi di Palermo, Italy

ARTICLE INFO

*Keywords:*
Roughness
Effective slope
LES
Channel flow

ABSTRACT

This study explores the effects of wall roughness density on turbulence characteristics through Large Eddy Simulations (LES). The roughness is modeled using Gaussian functions, and the focus is on how variations in roughness density influence higher-order statistical properties, such as Reynolds stresses and turbulence anisotropy. The findings show that rough walls cause a downward shift in the mean velocity profile, denoted as $\Delta U^+$, with turbulence becoming more isotropic as the roughness height increases. The study specifically examines the influence of roughness density by comparing configurations obtained through 32- and 64-Gaussian functions. The results indicate that increasing the roughness density from 32 to 64 elements leads to a smaller impact on the turbulent flow field. This outcome is consistent with previous work, where it was shown that, for the same mean height of roughness $k/h$, the reduction in the velocity profile becomes less pronounced as the roughness density increases. In other words, while an increase of the roughness height results in a larger shift in the velocity profile, the effect diminishes with increasing roughness density, as seen with the 64-Gaussian configuration compared to the 32-Gaussian one. In addition, the study investigates the influence of roughness on turbulent structures such as streaks and vortical formations. The results confirm that roughness modifies the spatial organization of turbulence, with increased roughness height leading to wider vortical structures and more intermittent streaks. These observations contribute to a better understanding of how surface roughness affects turbulence dynamics, highlighting the complex relationship between roughness density, flow behavior, and turbulence organization near rough walls.

## 1. Introduction

Turbulent flows over uneven surfaces are widespread in engineering contexts, ranging from designing airfoils to managing pipe flows. It is crucial to understand the complex association between irregular rough surfaces and turbulent flows, as it holds key significance in forecasting roughness function as well as skin friction. Despite extensive research over the years, accurately predicting these phenomena remains an ongoing challenge, primarily due to the intricate interplay between surface geometry and the dynamics of fluid flow. Wall roughness usually gives rise to significant skin friction, which increases turbulent flows and leads to a downward shift of the mean velocity profile. Hence, predicting the effect of rough walls on turbulence has become an important design prerequisite for practical applications. The foundational study on the skin friction coefficient in rough-wall turbulence was conducted by Nikuradse (1933). Through comprehensive measurements of pressure drops in pipes lined with sand grains, he demonstrated that, in the fully rough regime at sufficiently high Reynolds numbers, the skin friction coefficient is governed exclusively by an equivalent sand grain roughness. Further extensions of this work were performed by Colebrook et al. (1939), who investigated the skin friction coefficient for several industrial pipes. Moody (1944) consolidated those data into a Moody chart for practical engineering applications. The Moody chart is a powerful tool for estimating pressure loss due to wall roughness, provided that the equivalent roughness for the specific roughness type is known a priori, such as that of commercial steel pipes, glass and concrete. However, for naturally occurring roughness due to erosion, corrosion, or fouling processes, the equivalent roughness is usually unknown. Hence, many studies have dedicated their efforts to exploring the relation between equivalent roughness and roughness topology (see, among others: Schlichting, 1937; Sigal and Danberg, 1990; Van Rij et al., 2002). For the estimation of the equivalent roughness, Dirling (1973) proposed a roughness parameter that includes roughness density and a shape parameter. The roughness density was represented as the ratio of the average element spacing to roughness height, while the

---

* Corresponding author.
*E-mail address:* federica.bruno@unikore.it (F. Bruno).

https://doi.org/10.1016/j.ijheatfluidflow.2025.110126
Received 28 May 2025; Received in revised form 20 October 2025; Accepted 21 October 2025

| | |
|---|---|
| **English Symbols** | |
| $h$ | Channel half-width |
| $L_x, L_y, L_z$ | Streamwise, spanwise and wall-normal domain dimensions |
| $Re_b$ | Bulk Reynolds number |
| $Re_{cl}$ | Centerline Reynolds number |
| $Re_\tau$ | Friction Reynolds number |
| $t$ | Time |
| $U_{b^+}$ | Normalized bulk mean velocity |
| $U_{cl^+}$ | Normalized centerline mean velocity |
| $U_{i,sst}$ | Average velocity over streamwise, spanwise directions and time |
| $U_{i,st}$ | Average velocity over spanwise direction and time |
| $U_{i,t}$ | Average velocity over time |
| $u_\tau$ | Friction velocity |
| $x_1, x_2, x_3$ | Streamwise, spanwise, and wall-normal directions |
| $\bar{u}_1, \bar{u}_2, \bar{u}_3$ | Components of the filtered velocity field |
| $\bar{p}$ | Kinematic pressure field |
| $\Delta U^+$ | Roughness function |
| $g$ | Gravitational acceleration |
| **Greek Symbols** | |
| $\delta_{ij}$ | Kronecker delta |
| $\eta$ | Kolmogorov length scale |
| $\kappa$ | von Kármán constant |
| $\mu$ | Mean of the Gaussian distribution |
| $\nu$ | Kinematic viscosity |
| $\Pi$ | Imposed non-dimensional pressure gradient |
| $\rho$ | Fluid density |
| $\sigma$ | Standard deviation |
| $\tau_s$ | Wall stress |
| **Subscripts and Superscripts** | |
| $+$ | Non-dimensional variables |
| $()'$ | Variable fluctuation |
| **Abbreviations** | |
| 2D | Two-dimensional |
| 3D | Three-dimensional |
| AIM | Anisotropy Invariant Map |
| DNS | Direct Numerical Simulation |
| HMR | High Momentum Region |
| LES | Large Eddy Simulation |
| LMR | Large Momentum Region |
| rms | Root Mean Square |
| SGS | Subgrid-scale model |

shape parameter accounted for the frontal area and the windward wetted surface area of a single roughness element. In order to extend the applicability of the roughness parameter introduced by Dirling (1973), Sigal and Danberg (1990) replaced the roughness density with the ratio of the area of the smooth surface before adding the roughness and the total frontal area over the rough surface. Van Rij et al. (2002) proposed a more generalized form by replacing the shape parameter of Dirling (1973) with the ratio of the total frontal area to the total wetted area for all the roughness elements and reported that the proposed correlation could also be applicable to walls with non-uniform, three-dimensional roughness with irregular geometry and arrangement. One of the first attempts to find a mathematical law to predict the main roughness effect was given by Hama (1954), introducing the correlation between a parameter known as the equivalent sand grain roughness $k_s$ and the energy loss induced by the roughness. Hama (1954) focused attention on the downward shift of the mean velocity profile in the log region, known as Roughness Function $\Delta U^+$ (hereafter, the superscript $^+$ denotes variables made non-dimensional with inner variables $u_\tau = (\tau_s/\rho)^{0.5}$ and $\nu/u_\tau$, where $u_\tau$ is the friction velocity, $\tau_s$ is the wall stress, $\rho$ the fluid density and $\nu$ the kinematic viscosity). This shift is correlated with the equivalent sand grain roughness $k_s$ through the equation:

$$\Delta U^+ = \frac{1}{\kappa} ln(k_s^+) + B \tag{1}$$

where $\kappa$ is the von Kàrmàn constant, $k_s^+ = k_s \cdot u_\tau/\nu$ and B is a constant. Unfortunately, for a general rough wall, $k_s$ cannot be calculated a priori; it can be, in fact, determined once the mean velocity profile is known. In fact, as pointed out by several authors (see, among others: Flack et al., 2020), $k_s$ is not a physical measure of corrugation. Attention to the effect of roughness on turbulent flow has increased in the last few years, also in light of energy consumption and or turbomachinery efficiency. This can be well observed through the huge recent literature findings who focused the attention on the velocity estimation once the roughness is known (see, among others: Jalalabadi and Stoesser, 2022; Abdelaziz et al., 2022; Viggiano et al., 2022; Ganju et al., 2022; Ma et al., 2022; Aghaei-Jouybari et al., 2023; De Maio et al., 2023; Yang et al., 2023; Nair et al., 2024; Kuwata et al., 2024; Nair et al., 2024; Kuwata et al., 2024; Bruno et al., 2024a, and literature therein analyzed). More recently, Kaminaris et al. (2026), performed Direct Numerical Simulations to investigate on spatially developing boundary layers covered by synthesized biofouling-type roughness comprising both barnacle- and tubeworm-type organisms at a fixed planar and various frontal solidities. The results suggest that both the roughness function and the boundary layer growth, as well as the total drag evolution scale with the frontal area of the roughness. Further investigations on the total drag modification induced by the roughness, was recently carried out by Bruno et al. (2026). The authors proposed a new geometrical parameter, named the Effective Distribution (ED) and based on the Effective Slope ES of Napoli et al. (2008), showing that the contributions of higher pinnacles and the spacing between roughness elements play a dominant role in capturing the impact of roughness on drag and turbulent intensities. All these recent researches clearly confirm the importance to further investigate on the effect of corrugated walls on turbulent flows. In this study, Large Eddy Simulations were performed to replicate the rough wall using the same methodologies proposed by Bruno et al. (2024b), employing Gaussian functions. Expanding on this previous work, the proposed study delves deeper into examining the impact of roughness density on higher-order statistical properties. The paper is organized as follows: Section 2 describes the numerical procedure adopted for LES and flow configurations, the results are presented in 3 and the conclusions are drawn in 4.

## 2. Numerical methodology and modeling wall roughness

The analysis has been performed numerically by solving the mass and momentum conservation equations, for an incompressible Newtonian fluid:

$$\frac{\partial \bar{u}_i}{\partial t} + \frac{\partial \bar{u}_i \bar{u}_j}{\partial x_j} - \frac{1}{Re_\tau}\frac{\partial^2 \bar{u}_i}{\partial x_j \partial x_j} + \frac{\partial \bar{p}}{\partial x_i} + \frac{\partial \tau_{ij}}{\partial x_j} + \Pi\ \delta_{i1} = 0 \tag{2}$$

$$\frac{\partial \bar{u}_i}{\partial x_i} = 0 \tag{3}$$

where the variables are made non-dimensional with the friction velocity $u_\tau$ and the channel half-width $h$; $x_i$ is the $i$th coordinate (with $x_1$, $x_2$, and $x_3$ the streamwise, spanwise, and wall-normal directions, respectively), $t$ is the time, $\bar{u}_i$ is the $i$th component of the filtered velocity field, $\bar{p}$ is the kinematic pressure field (pressure divided by density and $u_\tau^2$), $\tau_{ij} = \overline{u_i u_j} - \bar{u}_i \bar{u}_j$ is the sub-grid scale turbulent stress tensor, $Re_\tau = u_\tau h/\nu$ is the frictional Reynolds number, $\Pi$ is the imposed non-dimensional pressure gradient to drive the flow, and $\delta_{ij}$ is the Kronecker function ($\delta_{ij} = 1$ for $i = j$, $\delta_{ij} = 0$ for $i \neq j$). In Eqs. (2) and (3), the symbol $\bar{\cdot}$ denotes filtered quantities. The subgrid-scale (SGS) stress tensor $\tau_{ij}$ is modeled using the Dynamic Mixed Model (DMM) of Zang et al. (1993). The momentum and continuity Eqs. (2)

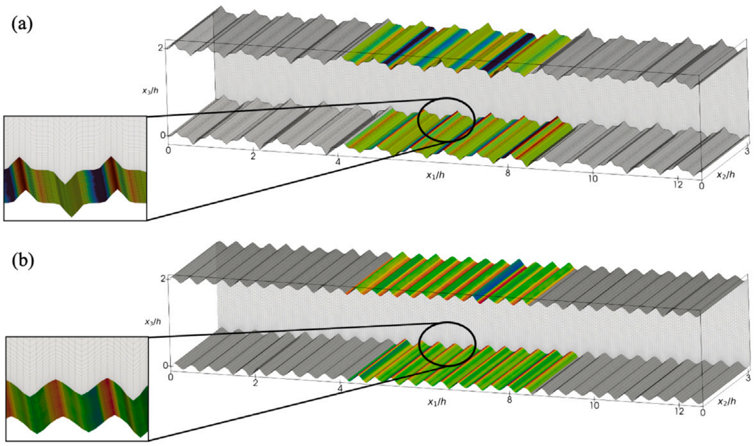

**Fig. 1.** 3D sketch of the computational domain for two configurations. (a) with 32-Gaussian functions, (b) 64-Gaussian functions.

and (3) are solved using the finite-volume numerical code PANORMUS, which is second-order accurate both in time and space (Napoli et al., 2008). The Adams–Bashforth method is used as the time advancement scheme, whereas a fractional-step technique is applied to overcome the pressure–velocity decoupling typical of incompressible flows. The pressure Poisson equation is solved through a line-SOR technique in conjunction with a multigrid V-cycle accelerator, thus ensuring fast convergence. Further details on the numerical procedure can be found in De Marchis (2016), Milici and De Marchis (2016), De Marchis et al. (2019). Numerical simulations were performed to replicate the rough wall using the methodologies proposed by Bruno et al. (2024b), employing Gaussian functions. In their study, Bruno et al. (2024b) examined the impact of roughness density and coverage on mean flow. Specifically, for lower roughness density (32-Gaussian curves), a higher downward shift of the velocity was observed compared to cases with higher roughness density (64-Gaussian curves). A symmetrical channel was built imposing the roughness both on upper and lower walls, designed through the following equation. Both walls were generated using:

$$k[x_1(ii)] = \sum_{i=1}^{32\cdot jj} \beta \sum_{j=1}^{8/jj} \frac{1}{\sigma_i\sqrt{2\pi}} e^{-\frac{1}{2}\left(\frac{x_1(j)-\mu}{\sigma_i}\right)^2} \tag{4}$$

Here, $k[x_1(ii)]$ represents the roughness height at the streamwise coordinate $x_1(ii)$ obtained through the superposition of Gaussian functions, where $x_1$ is the streamwise position, $\sigma_i$ is the standard deviation. Each $\sigma_i$ is randomly selected from a uniform distribution in the range $B < \sigma_i < 1 + B$, where $B$ is a constant specific to the geometry. The coefficient $\beta$ takes the value $+1$ if $i$ is even and $-1$ if $i$ is odd. The indices are defined as $ii = i \cdot j$, and $jj = 1$ for cases with 32-Gaussian functions, while $jj = 2$ for cases with 64-Gaussians. The variable $\mu$ denotes the mean of the Gaussian distribution, which also coincides with its median and mode, and it is kept constant at $\mu = \frac{4\pi}{16}$.

Due to the randomness in $\sigma_i$, the upper and lower walls exhibit different shapes, although they share the same statistical characteristics. Fig. 1 shows a 3D sketch of the computational domain for two configurations: one with 32-Gaussian functions and one with 64.

The computational domain is a typical turbulent channel measuring $4\pi h \times \pi h \times 2h$ in the $x_1$, $x_2$, and $x_3$ directions, respectively. In both flat and rough conditions, to simulate the channel flow, periodic boundary conditions are applied in both the streamwise and spanwise directions, while no-slip boundary conditions are enforced at the rough walls. The domain is discretized using curvilinear, structured, boundary-fitted grids, as visible in the inset plotted in Fig. 1. All the simulations are performed at a friction Reynolds number of $Re_\tau = 400$. The geometrical and flow properties are summarized in Table 1. The adequacy of the computational domain in both the streamwise and spanwise directions has been verified using two-point correlations, which fall to zero at a distance shorter than half the domain length, confirming that the domain is sufficiently large to resolve all elongated structures. The analysis of the two-point correlation is discussed in the following sections.

It is known (see, among others: Piomelli and Balaras, 2002; Choi and Moin, 2012, and literature citing them) that a streamwise grid spacing of $\Delta x_1^+ \approx 50$–$100$ and spanwise spacing $\Delta x_2^+ \approx 30$ wall units is a sufficient requirement to resolve large-scale structures in LES. In rough conditions a further grid refinement is suggested (see, De Marchis et al., 2010) due to the roughness-induced disruption of elongated turbulence structures, causing a reduction of their length scale. In order to ensure an elevated resolution of these coherent structures, here the dimension of the grid cells is set to $\Delta x_1^+ = \Delta x_2^+ \approx 19.6$, uniformly distributed, due to the periodic boundary condition. In the vertical direction, on the other hand, a non-uniform mesh spacing is imposed. Specifically, a refinement is required close to the lower and upper walls, ensuring a minimum wall-normal spacing of $\Delta x_{3,\min}^+ = 0.5$ and it gradually increases towards the channel centerline, reaching a maximum of $\Delta x_{3,\max}^+ = 26.5$. The resulting number of grid cells is $256 \times 64 \times 64$ in the streamwise, spanwise and wall-normal directions, respectively. The resolution is finer than these LES recommendations and closer to DNS standards (where $\Delta x_1^+ \approx 7$–$8$ is common). The chosen resolution was tested through sensitivity tests, carried out by repeating selected simulations on progressively refined grids, not shown here, confirming the adequacy of the mesh resolution. Additional validations on a wide range of cases was performed ensuring the adequacy of the domain and the of the numerical code. Details on the validation of the proposed numerical model are discussed in the following section.

## 3. Results and discussion

The effect of two sets of rough geometries on turbulent flow is analyzed through both quantitative analyses, based on the mean quantities, and qualitative analyses, based on turbulent fluctuating and instantaneous fields. Due to the different nature of the analyzed results, different types of averages are required. Specifically, the mean streamwise velocity profile can be obtained in three different ways. The first approach involves averaging over both streamwise and spanwise directions as well as time, resulting in statistical quantities along the vertical direction (i.e., velocity profiles) and can be expressed as $U_{i,sst} = \langle u_i(x_1, x_2, x_3, t)\rangle_{sst}$, where the subscript $_{sst}$ indicates Streamwise, Spanwise, Time. Alternatively, averaging can be performed over time and in the spanwise direction, yielding contour mean values along $x_1$-$x_3$ planes, which is particularly suitable for 2D rough surfaces and is defined as $U_{i,st} = \langle u_i(x_1, x_2, x_3, t)\rangle_{st}$. Finally, averaging over time alone allows for the calculation of averaged 3D flow fields, as described by

**Table 1**

Flow properties of the numerical simulations. $Re_\tau$, $Re_{cl}$ and $Re_b$ are the friction, centerline, and bulk Reynolds number. $U_{cl^+}$ is the normalized centerline mean velocity, $U_{b^+}$ is the normalized bulk velocity. $\Delta U^+$ is the Hama Roughness Function, and $\overline{k^+}$ is the mean roughness height given by $\overline{k}^+ = \frac{\overline{k} u_\tau}{\nu} = \left(\frac{\overline{k}}{h}\right) Re_\tau$, where $\overline{k} = \frac{1}{n}\sum_{i=1}^{n} |x_{3,i}|$ .

| *Marker* | *Sketch* | *Case* | *NG* | $Re_\tau$ | $Re_{cl}$ | $Re_b$ | $U_{cl^+}$ | $U_{b^+}$ | $U_{cl^+}/U_{b^+}$ | $\Delta U^+$ | $\overline{k^+}$ |
|---|---|---|---|---|---|---|---|---|---|---|---|
| ● |  | 32_0.5 | 32 | 400 | 7443 | 6427 | 18.61 | 16.07 | 1.16 | 1.65 | 2.00 |
| ● |  | 32_1 | 32 | 400 | 5980 | 5030 | 14.95 | 12.57 | 1.19 | 5.12 | 3.98 |
| ● |  | 32_2 | 32 | 400 | 3960 | 3095 | 9.90 | 7.74 | 1.28 | 9.91 | 7.98 |
| ● |  | 32_3 | 32 | 400 | 3000 | 2129 | 7.50 | 5.32 | 1.41 | 12.55 | 11.98 |
| ● |  | 32_4 | 32 | 400 | 2504 | 1686 | 6.26 | 4.21 | 1.49 | 13.31 | 15.98 |
| ◆ |  | 64_0.5 | 64 | 400 | 7588 | 6553 | 18.97 | 16.38 | 1.16 | 1.41 | 2.00 |
| ◆ |  | 64_1 | 64 | 400 | 6181 | 5175 | 15.45 | 12.94 | 1.19 | 4.87 | 3.98 |
| ◆ |  | 64_2 | 64 | 400 | 4760 | 3824 | 11.90 | 9.56 | 1.24 | 8.33 | 7.98 |
| ◆ |  | 64_3 | 64 | 400 | 3971 | 3067 | 9.93 | 7.67 | 1.29 | 10.17 | 11.98 |
| ◆ |  | 64_4 | 64 | 400 | 3391 | 2517 | 8.48 | 6.29 | 1.35 | 11.24 | 15.98 |

$U_{i,t} = \langle u_i(x_1,x_2,x_3,t)\rangle_t$. Once the appropriate averaging method has been selected, the corresponding turbulent velocity fluctuations can be calculated. In particular, the resolved turbulent velocity fluctuations for the fully space- and time-averaged velocity are given by $u'_{i,sst} = u_i(x_1,x_2,x_3,t) - U_{i,sst}$, which represents the deviation from the overall mean. In the case of time and spanwise averaging, the fluctuations are defined as $u'_{i,st} = u_i(x_1,x_2,x_3,t) - U_{i,st}$ capturing deviations from the mean flow on 2D rough surfaces. Finally, for purely time-averaged data, the fluctuations are calculated as $u'_{i,t} = u_i(x_1,x_2,x_3,t) - U_{i,t}$.

### 3.1. Numerical validation

According to several authors (see, among others: Vreman et al., 1996; Celik et al., 2005) two main approaches are commonly used to assess the performance of SGS (subgrid-scale) models:

- A priori tests, in which model predictions are compared with SGS stresses obtained from DNS or experiments through filtering;
- A posteriori tests, in which LES results are directly compared with those from DNS or experiments.

Some authors (see, Vreman et al., 1996) criticize the a priori testing procedure, arguing that it often leads to poor prediction of turbulent quantities, although this does not necessarily imply poor LES performance. Similarly, Pope (2000) notes that models performing poorly in a priori tests may still yield satisfactory results in a posteriori tests. Here, the validation was performed using the second approach given by a comparison between our results with the previous ones. Specifically, the reliability of the numerical code in simulating turbulent channel flow has been established through systematic comparisons with the available DNS datasets. The code has been extensively validated under smooth wall conditions up to a friction Reynolds number of $Re_\tau = 1000$ (see, De Marchis et al., 2020). Here, a validation on rough wall conditions is reported. However, since no experimental or DNS data are available for Gaussian roughness, an additional validation was performed on a rough-wall case for which DNS data exist, namely the large-amplitude wavy wall of Maaß and Schumann (1996). Fig. 2 reports the comparison of mean velocity profiles and turbulence intensities. The LES results show very good agreement with the DNS data, confirming the capability of the proposed model to reproduce turbulent flow dynamics also under rough-wall conditions. Furthermore, the model has been extensively and favorably validated over a wide range of flow configurations (see, Napoli et al., 2008; De Marchis et al., 2010; De Marchis and Napoli, 2012; De Marchis, 2016). However, the a posteriori approach is affected by the well-known difficulty in distinguishing between numerical (or discretization) errors and modeling errors (see, among others: Meneveau, 1994), which complicates the determination of the turbulent energy dissipation rate introduced by the SGS model. In general, the total error, and thus the uncertainty in LES, consists of two major components: the numerical discretization error ($\varepsilon_{num}$) and the modeling error, i.e., the subgrid-scale model error ($\varepsilon_{SGS}$). The numerical discretization error can be minimized using fine grid resolution, so attention is focused on the SGS error. In order to give a quantitative analysis on the subgrid-scale error, the SGS effect was estimated through the ratio between the resolved and the total stresses. In smooth conditions, the mean resolved stresses are about 90% of the total stresses, with a minimum of about 87% observed close to the peak of the turbulent intensities and a maximum of 93% in the central part of the channel. In rough conditions similar results were achieved. Specifically, the mean resolved stresses are about 85% of the total stresses for the highest roughness cases. The results confirm the ability of the proposed numerical simulations to capture the behavior of turbulent flows on rough surfaces.

### 3.2. Mean velocity profile

The effect of surface roughness is to shift the mean velocity profile downward, compared to that on a smooth wall, by an increment denoted as $\Delta U^+$. Consequently, the following results focus on the influence of corrugated walls on velocity reduction. Henceforth, all the statistical quantities presented are non-dimensionalized using the friction velocity $u_\tau$. In the following figures, the non-dimensional wall distance $x_3^+$ is measured from the flat reference plane, upon which Gaussian functions are superimposed to create the wall roughness. Figs. 3a–b illustrate the mean velocity profiles in the streamwise direction obtained from all numerical simulations carried out at $Re_\tau = 400$, as reported by Bruno et al. (2024b).

In Fig. 3a, the results for simulations with 32-Gaussian-shaped roughness elements are shown. As expected, the figure clearly demonstrates an increase in the downward shift of the velocity profile with an increase in mean roughness height, $\overline{k}$, from $0.005 \cdot h$ to $0.04 \cdot h$. Fig. 3b shows the mean velocity profiles obtained over irregular rough surfaces characterized by a density of 64-Gaussian elements. Bruno et al. (2024b) confirmed that the roughness height increases, correlates with a larger roughness function. This behavior can be attributed to enhanced energy dissipation caused by wall oscillations. Interestingly, all profiles exhibit the same slope regardless of the roughness conditions, corresponding to the classical von Kàrmàn constant, thereby ensuring the validity of the log-law region. In contrast with previous works (see, for example: De Marchis et al., 2010), differences from the smooth wall case are observed both in the inner and outer layers, with these differences increasing with mean roughness height. These findings align with those of other studies (e.g., Chung et al., 2021; Flack and Schultz, 2014), which suggest that similarity holds only for large separations. In the near-wall region, the plots reveal that the 32 roughness produces a more pronounced velocity reduction compared to the 64 roughness. Although the mean roughness height $\overline{k}^+$ is the same for 32- and 64-Gaussian cases at each $\overline{k}/h$ value (e.g., $\overline{k}^+ = 15.98$ for both 32_4 and 64_4), the maximum roughness height $k^+_{max}$ is higher in the 32-Gaussian

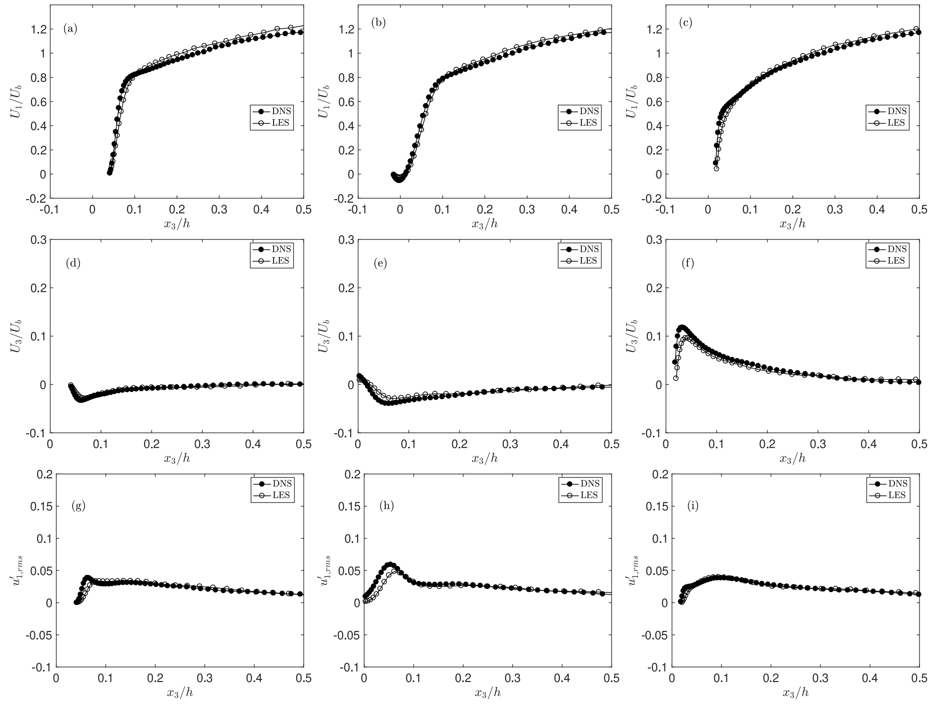

**Fig. 2.** Comparison between LES results and DNS data from (Maaß and Schumann, 1996). (a–c) Streamwise mean velocity profiles at $x/\lambda = 0.1015$, 0.3046, and 0.8046, respectively. (d–f) Wall-normal mean velocity profiles at $x/\lambda = 0.1015$, 0.3046, and 0.8046, respectively. (g–i) Streamwise root-mean-square (rms) of velocity fluctuations at $x/\lambda = 0.1015$, 0.3046, and 0.8046, respectively.

cases. This indicates that the 32-Gaussian roughness has taller peaks that can penetrate more into the log and outer layers, particularly in cases with highest roughness (e.g., 32_4). However, the difference in $\Delta U^+$ and Reynolds stresses between 32- and 64-Gaussian cases is primarily associated with the increase in roughness density, rather than the maximum peak height. This observation is consistent with the findings of Bruno et al. (2024b), who showed that the contribution of roughness elements to drag depends on their pattern and distance from upstream elements, and that elements located in the wake of larger peaks have a negligible effect. Furthermore, the spacing between consecutive roughness elements influences the velocity distribution, the momentum within the cavities, and the intensity of the stagnation point on the windward element. Therefore, the higher density of Gaussian elements in the 64-Gaussian case distributes the roughness more evenly, reducing the influence of extreme peaks on the flow. In summary, the increase in roughness density dominates the observed differences between 32- and 64-Gaussian cases, while the slightly higher maximum roughness heights in the 32-Gaussian cases may contribute to minor secondary effects on local turbulent interactions. The results, both for 32 and 64, are consistent with the findings of various authors (Antonia and Krogstad, 2001; Ashrafian et al., 2004; Bhaganagar et al., 2004; Lee et al., 2011) demonstrating that outer-layer independence of surface roughness is observed only at lower roughness heights. As roughness increases, this similarity disappears. To gain further insight into how roughness affects the reduction in velocity profiles, Fig. 4 present contour plots depicting the streamwise average velocity $U_{1,t}$ across the $x_1 - x_3$ plane, plotted in the middle of the channel ($x_2/h = \pi/2$) for each analyzed case. These visualizations provide a detailed understanding of the flow dynamics, illustrating the impact of various roughness conditions on turbulent flow behavior. As the mean roughness increases, recirculating flows become evident within the cavities. For walls with 32-Gaussian roughness elements, wider vortical eddies are observed. These results reaffirm that 32 roughness leads to a more significant reduction in velocity compared to 64 roughness.

### 3.3. Reynolds stresses

Although the roughness function is an effective tool for assessing the impact of roughness on the flow field, it is essential to extend the analysis to other important turbulent quantities, such as Reynolds stresses. This is motivated by the need to evaluate the influence of roughness in the inner layer, where Reynolds stresses serve as valuable indicators. In this section, the root mean square (rms) of velocity fluctuations, denoted as $u'_{i,rms}$, is analyzed. Fluctuations $u'_{i,rms}$ were calculated using the velocities averaged in the spanwise direction and over the time only $u'_{i,st}$.

Figs. 5 (a-b) present the vertical profiles of non-dimensional root mean square values of streamwise velocity fluctuations ($u'_{1,rms}$ or $\sqrt{u'_1 u'_1}$), averaged over time and the $x_1 x_2$-planes. A smooth-wall profile is included for comparison. These profiles represent the total fluctuations, incorporating contributions from both resolved and subgrid-scale turbulence. As the roughness height increases, the amplitude of these profiles gradually decreases, with this trend noticeable even for low roughness heights ($\overline{k} = 0.005 \cdot h$). For higher roughness heights, such as $\overline{k} = 0.04 \cdot h$, the profiles become nearly flat. The effects of roughness are mainly confined to the initial 100 wall units, with turbulent intensities, represented by the square root of the normal Reynolds stresses, diminishing in the outer flow region. Notably, the collapse of rms velocity fluctuation profiles in the outer region is essentially limited to the streamwise component and only partially extends to other components, as shown in Figs. 5 (c-d) and 5 (e-f). However, in the inner layer, there is a general increase in velocity fluctuations. This redistribution indicates a trend towards more isotropic near-wall turbulent scales. In other words, the turbulence near the wall becomes less dominated by streamwise directionality and is more evenly distributed across all directions. In contrast to the other two velocity components, the rms of wall-normal velocity fluctuations shows deviations from the smooth-wall case even in the inertial region, especially in the fully rough cases (32_4 and 64_4). These deviations result from the progressive increase in the instantaneous wall-normal velocity induced by the peaks of wall

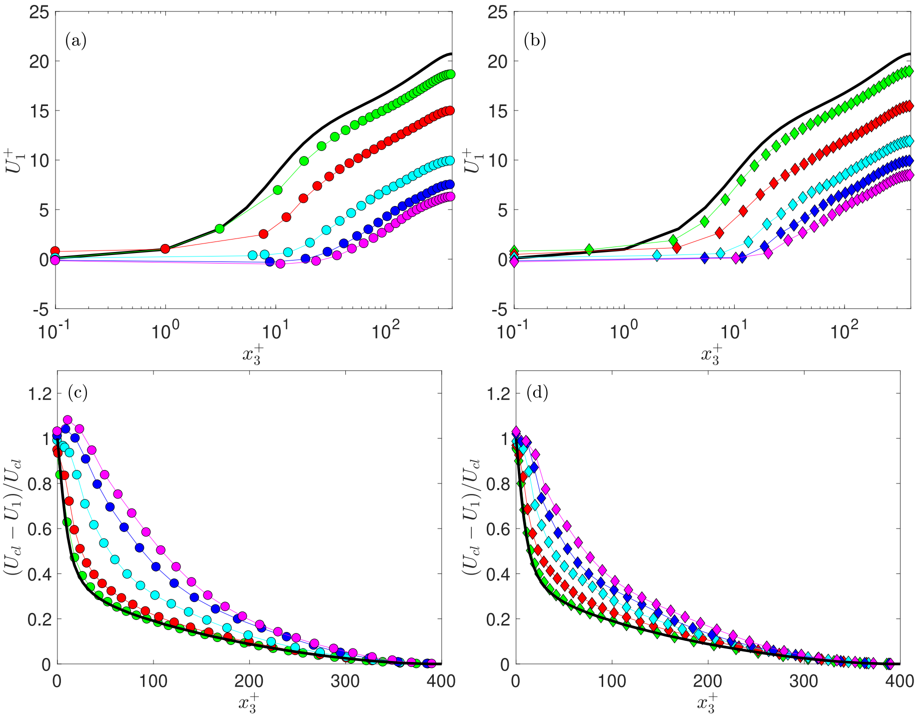

**Fig. 3.** (a) Mean streamwise velocity $U_{1,sst}$ profile for the smooth wall and rough cases 32. (b) Mean streamwise velocity profile for the smooth wall and rough cases 64. (c) Mean velocity defect profile for the smooth wall and rough cases 32. (d) Mean velocity defect profile for the smooth wall and rough cases 64. Color and symbols are referred to Table 1.

roughness. As noted by Orlandi et al. (2003) and De Marchis et al. (2010), this effect may enhance interactions between the roughness elements and the surrounding external flow.

The findings presented here hence only partially support Townsend's wall similarity hypothesis (1976), which asserts that, at sufficiently high Reynolds numbers, turbulence beyond the roughness layer becomes independent of specific wall conditions. However, inner/outer layer interactions are evident in the wall-normal velocity component, particularly for fully rough surfaces. This observation is consistent with the analysis by Bhaganagar et al. (2004), who suggested that the extent of inner/outer-layer interactions may depend on the size and characteristics of the roughness elements. An increase in the height of the roughness leads to a reduction in both Reynolds stresses and viscous shear stress, which collectively result in a rise in the mean velocity profile within the near-wall region. Physically, more pronounced recirculation phenomena occur beyond the roughness height, enhancing vertical mixing and thereby reducing the viscous contribution. As noted by Miyake et al. (2002) and Coceal et al. (2006), the total stress grows linearly from the channel centerline towards the wall (similar to smooth channel flows) but deviates at a distance from the wall corresponding to the roughness height. Below the roughness crest, deviations from linearity are offset by the pressure stress acting on the surface, which increases with roughness height. Figs. 6 (a-f) display the profiles of turbulent shear stress $(u'_1 u'_3)$ in viscous units. In the figure the viscous stress $\nu \frac{\partial U_1}{\partial x_3}$ is also reported. The trend of total tangential stress $\tau_{tot}$ is also depicted as a dashed line, derived from the sum of the contribution of viscous, turbulent, dispersive (obtained as $(\widetilde{u_1}\widetilde{u_3})$, with $\widetilde{u}_i = (u_{i,t}) - (u_{i,sst})$,) and pressure stress. The linearity of $\tau_{tot}$ confirms the statistical steady-state of the numerical simulations and indicates that the selected averaging period (100 non-dimensional time units) is sufficient for analyzing the turbulent flow. As the mean roughness height increases from $\overline{k} = 0.005 \cdot h$ to $\overline{k} = 0.04 \cdot h$, a rapid reduction in viscous stress is observed, with the Reynolds shear stress dominating the total stress. Additionally, comparisons between the 32- and 64-Gaussian rough surfaces reveal higher turbulent shear stress for lower-density roughness distributions. Although this difference is negligible for cases with $\overline{k} = 0.005 \cdot h$ and $\overline{k} = 0.1 \cdot h$, it becomes increasingly significant as the roughness height grows.

### 3.4. Reynolds stress anisotropy

#### 3.4.1. Anisotropy tensor

As suggested by several authors (see, among others: Antonia and Krogstad, 2001; Leonardi et al., 2006; De Marchis et al., 2010), the ratio between the Reynolds stresses is a suitable indicator to check the turbulence isotropy. It is well known, in fact, that the roughness induces a tendency towards turbulence isotropy close to the walls. To this aim, the normalized Reynolds stress anisotropy tensor provides a measure of local anisotropy, which describes how turbulence changes in direction within a fluid flow. This tensor is derived from the Reynolds stress tensor and is defined as:

$$b_{ij} = \frac{(u'_i u'_j)_{sst}}{(u'_i u'_i)_{sst}} - \frac{1}{3}\delta_{ij} \qquad (5)$$

where $(u'_i u'_i)_{sst}$ represents twice the turbulent kinetic energy (TKE). The tensor $b_{ij}$ is a symmetric and traceless tensor, bounded by $-\frac{1}{3} \leq b_{ij} \leq \frac{2}{3}$, and is zero for isotropic turbulence. Previous studies on anisotropy in boundary-layer flows over rough and smooth walls Shafi and Antonia (1995), Mazouz et al. (1998), Djenidi et al. (1999), Antonia and Krogstad (2001), De Marchis et al. (2010) have reported a reduction in anisotropy for rough-wall boundary layers compared to smooth-wall cases. These investigations also highlight the ability of surface roughness to redistribute turbulent energy more uniformly among the three velocity components. Mazouz et al. (1998) measured turbulence intensities in smooth and rough channels with k-type rod roughness. Their findings indicated that wall roughness increases the magnitude of the wall-normal anisotropy component, $b_{33}$, across the entire channel. Conversely, Shafi and Antonia (1995) observed the opposite trend in their analysis of rough-wall turbulent boundary layers, where $b_{33}$ was diminished. Similarly, Smalley et al. (2002) reviewed multiple

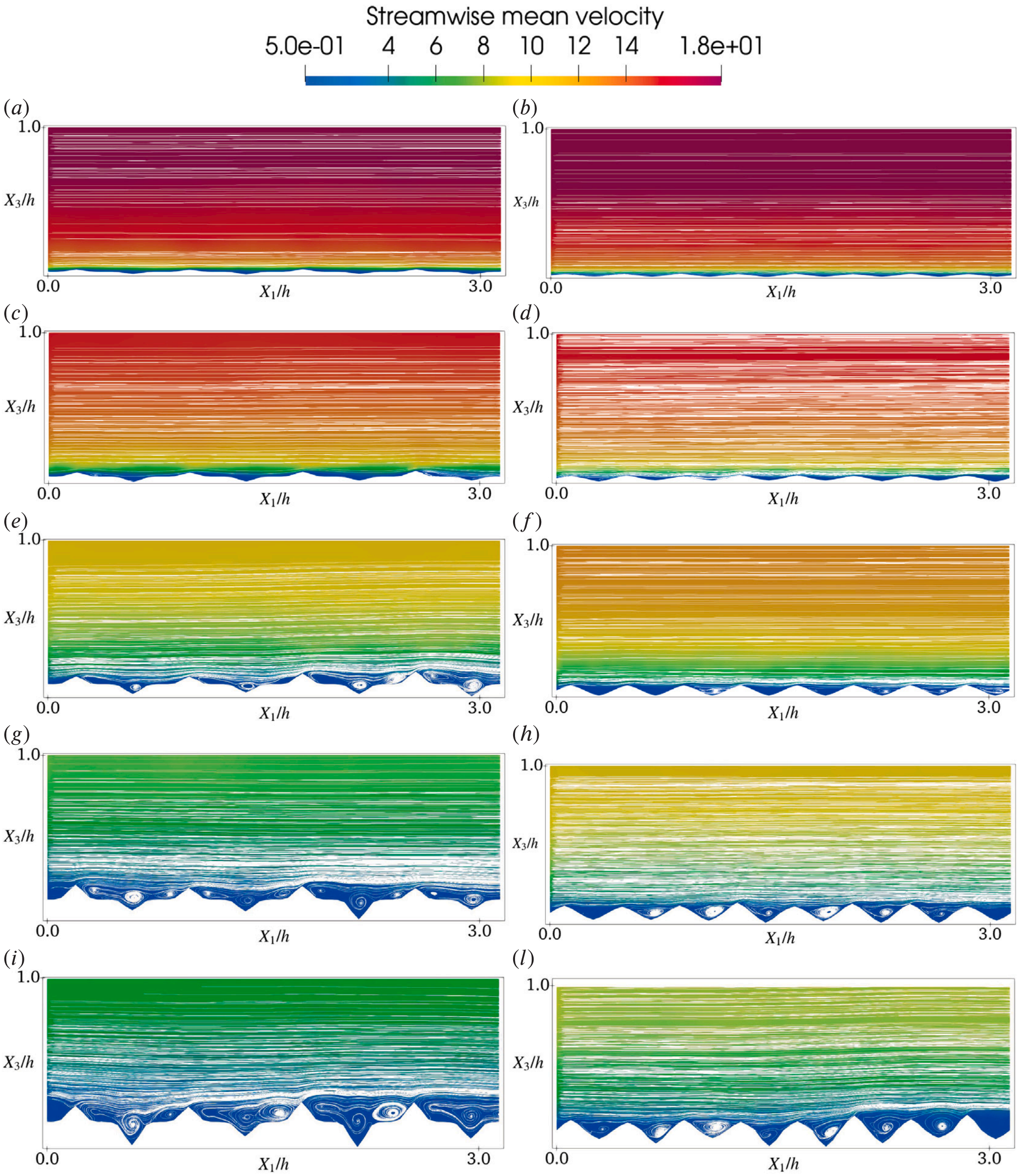

**Fig. 4.** Contours of the streamwise-averaged velocity $U_{1,t}$ in the $x_1$–$x_3$ plane at $x_2/h = \pi/2$, for the following cases: (a) 32_0.5; (b) 64_0.5; (c) 32_1; (d) 64_1; (e) 32_2; (f) 64_2; (g) 32_3; (h) 64_3; (i) 32_4; (l) 64_4.

datasets from previous rough-wall boundary-layer experiments, identifying variations in $b_{ij}$ for smooth and rough-wall cases. Fig. 7 illustrate the variations in the Reynolds stress anisotropy tensor components across smooth and rough surfaces to better understand the impact of roughness on turbulence anisotropy. For smooth walls, $b_{11}$ is positive, while $b_{22}$ and $b_{33}$ are negative, reflecting the dominance of streamwise velocity fluctuations over spanwise and wall-normal components. In contrast, for rough-wall cases, a consistent reduction in all diagonal components ($b_{11}$, $b_{22}$, $b_{33}$) is observed, indicating a roughness-induced isotropization of the turbulence scales. The reduction in anisotropy is negligible for the cases with $\overline{k} = 0.05 \cdot h$ and $\overline{k} = 0.1 \cdot h$, but becomes significant as the roughness height increases. For roughness cases with $\overline{k} = 0.2 \cdot h$, $\overline{k} = 0.3 \cdot h$, and $\overline{k} = 0.4 \cdot h$, the spanwise component $b_{22}$ undergoes a notable change, becoming positive near the wall, in contrast to its negative values for both the smooth-wall case and rough walls with lower roughness heights. This transition underscores the complex influence of roughness height on turbulence anisotropy, particularly in the near-wall region.

These findings align with the results reported for regular rough walls by Leonardi et al. (2004), Ashrafian et al. (2004). The analysis confirms that the 32-Gaussian roughness is more effective than its 64-Gaussian counterpart in reducing turbulence anisotropy. The deviations of the $b_{ii}$ terms from the smooth-wall case are more pronounced for the 32-Gaussian roughness, both in the inner and outer regions, resulting in nearly flat profiles. Similar trends were observed by Antonia and Krogstad (2001) when comparing rod and wire-mesh rough surfaces and by De Marchis and Napoli (2012) in the context of 2D versus 3D roughness.

### 3.4.2. *Anisotropy invariant map*

The tendency towards greater isotropy induced by the 32-Gaussian roughness is more clearly illustrated in Fig. 8, which depicts the Anisotropy Invariant Map (AIM) introduced by Lumley (1979). Shafi and Antonia (1995) compared the $b_{ij}$ components for turbulent boundary layers over wire-mesh roughness and smooth walls, finding a

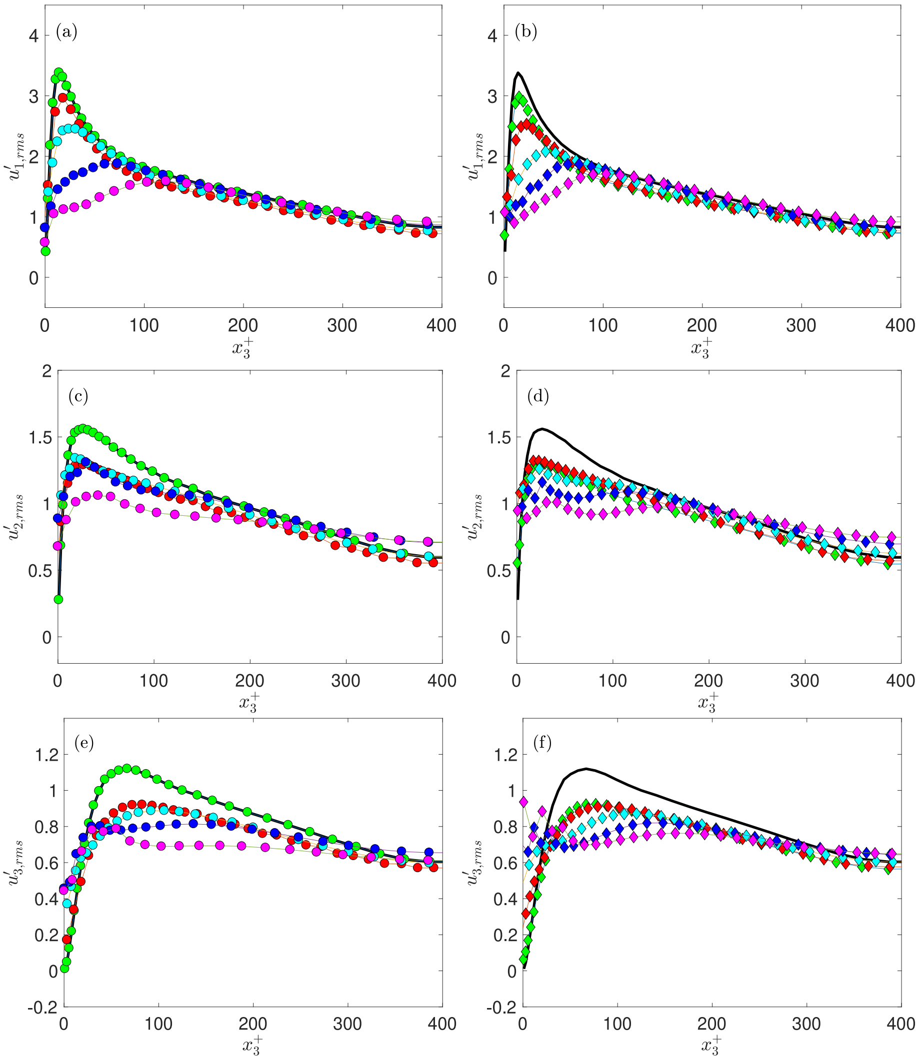

**Fig. 5.** Profiles of the root-mean-square (rms) velocity fluctuation components for the cases studied: (a, b) streamwise component $u'_{1,\mathrm{rms}} = \sqrt{u'_1 u'_1}$ for cases 32 and 64, respectively; (c, d) spanwise component $u'_{2,\mathrm{rms}} = \sqrt{u'_2 u'_2}$ for cases 32 and 64, respectively; (e, f) wall-normal component $u'_{3,\mathrm{rms}} = \sqrt{u'_3 u'_3}$ for cases 32 and 64, respectively. Colors and symbols correspond to those in Table 1.

significant reduction in anisotropy throughout the layer under rough-wall conditions. Similarly, AIMs for transverse square-cavity roughness (Djenidi et al., 1999) and rod roughness (Antonia and Krogstad, 2001) demonstrated a consistent reduction in anisotropy, reflecting the ability of rough surfaces to distribute turbulent energy more evenly among the three velocity components. Fig. 8 presents the AIM results for smooth and rough-wall cases.

The AIM is the cross-plot of the invariants $\xi$ and $\eta$ of the Reynolds stress anisotropy tensor defined as:

$$\xi = \left(\frac{\mathrm{III}_b}{2}\right)^{1/3}, \quad \eta = \left(-\frac{\mathrm{II}_b}{3}\right)^{1/2}, \tag{6}$$

where $\mathrm{II}_b = \frac{b_{ij}b_{ji}}{2}$, $\mathrm{III}_b = \frac{b_{ij}b_{jk}b_{ki}}{3}$. The turbulent states inside the Lumley triangle are bounded by: (a) an upper curve defined by the function $F = 1 - 27\eta^2 + 54\xi^3 = 0$, describing a two-component turbulence; (b) a straight line with negative values of $\xi$ defined by $\eta = -\xi$ corresponding to *disk-like* turbulence (in which two diagonal components of the anisotropy Reynolds stress tensor are greater than the third one).

For the reference smooth-wall case, the flow near the wall exhibits a tendency towards a two-component state, following the upper boundary of the Lumley triangle towards the one-component limit in the upper-right corner, where $u_1'^2$ is the dominant normal stress component. Maximum anisotropy is reached at $x_3^+ \approx 10$. Beyond this point, anisotropy decreases, with the $(\eta, \xi)$ curve tracking the right boundary of the triangle, indicating a near-axisymmetric, rod-like state. As $x_3^+$ increases further, the flow approaches the isotropic state at the bottom vertex of the triangle. These trends are consistent with the DNS data of Kim et al. (1987), which showed similar behavior at $x_3^+ \approx 7$ from the flat plane. Within the inner layer of the smooth-wall case ($5 < x_3^+ < 50$), $u_1'^2 \gg u_2'^2$ and $u_3'^2 > u_2'^2$, causing the AIM trajectory to follow the rod-like turbulence limit. The vortical structures near the viscous sublayer edge are elongated in the streamwise direction, reinforcing this behavior. For the 32- and 64-Gaussian rough walls with $\overline{k} = 0.005 \cdot h$ and $\overline{k} = 0.01 \cdot h$, the AIM trajectory reaches the left side of the triangle (Figs. 8a-d). At higher roughness heights ($\overline{k} = 0.02 \cdot h$), the trajectory approaches the left boundary below the roughness mean plane (Figs. 8e-f). In the roughness mean plane, the turbulence returns to a state closer to the right boundary, resembling smooth-wall behavior. For larger roughness heights ($\overline{k} = 0.03 \cdot h$ and $\overline{k} = 0.04 \cdot h$; Figs. 8g-l), turbulence states are scattered across the Lumley triangle. In the deepest surface valleys, the Reynolds stress anisotropy tensor closely resembles a highly anisotropic, one-component state. As $x_3^+$ increases, the flow transitions towards the left boundary, attaining an axisymmetric disk-like (oblate

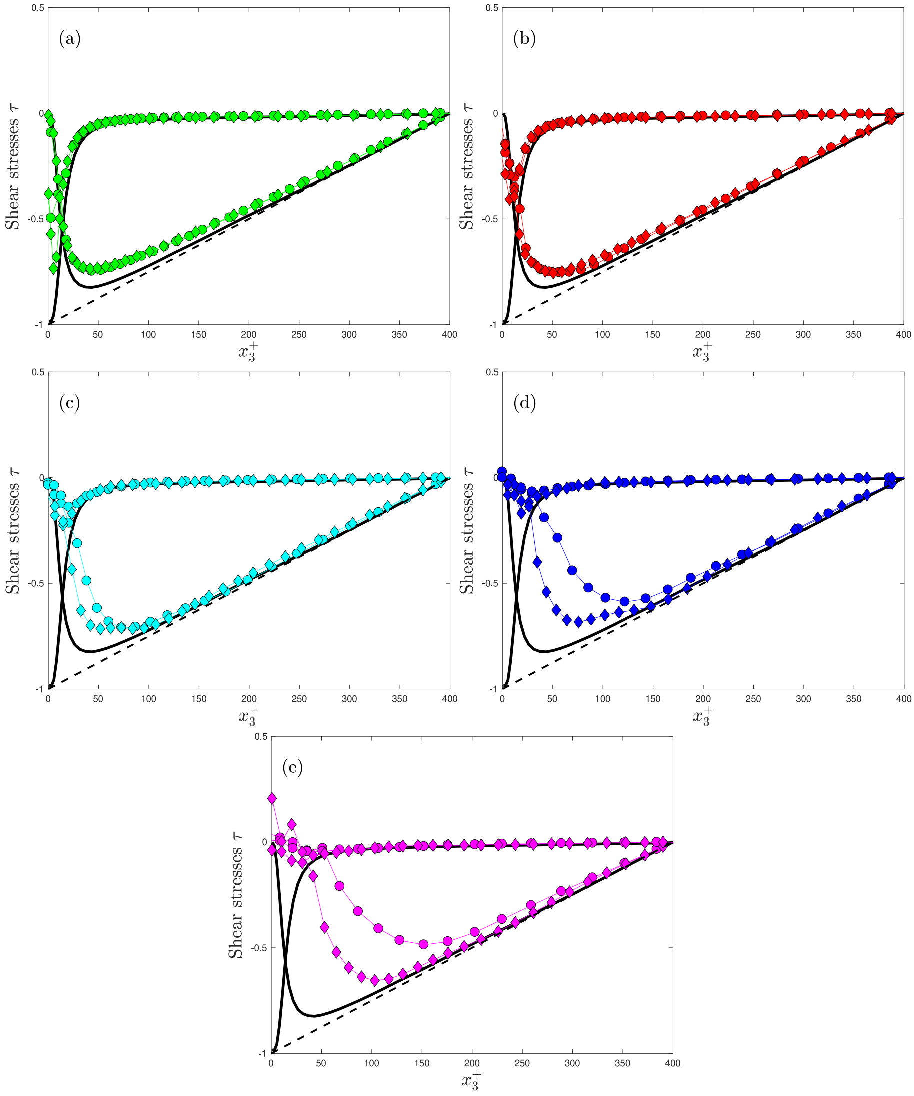

**Fig. 6.** Profiles of the Reynolds shear stress $(u_1' u_3')_{sst}$, viscous stress $\nu \frac{\partial U_{1,sst}}{\partial x_3}$, and total stress $\tau_{tot}$ for 32- and 64-Gaussian roughness cases: (a) $\overline{k} = 0.005\,h$; (b) $\overline{k} = 0.01\,h$; (c) $\overline{k} = 0.02\,h$; (d) $\overline{k} = 0.03\,h$; (e) $\overline{k} = 0.04\,h$. Bold line: smooth case; symbols: rough cases; dashed line: total stress.

spheroid) state at the roughness mean plane. Beyond the maximum roughness height, the trajectory shifts back towards the right boundary, mimicking the characteristics of the smooth-wall channel flow. Similar behavior has been observed in turbulent flows over transverse bar roughness (Ashrafian and Andersson, 2006; Varma et al., 2021), k-type roughness (Smalley et al., 2002), irregular roughness (Busse and Jelly, 2020) and additively manufactured rough surfaces (Garg et al., 2023). In Fig. 8, for the shake of clarity, two yellow markers are plotted. The first indicates the value at $y^+ = 0$, whereas the second indicates the location of maximum streak elongation. This clearly links streak elongation with the AIM trajectory, showing how elongated near-wall vortices lead to high anisotropy, and how turbulence becomes more isotropic or axisymmetric further from the wall. Overall, the 32-Gaussian roughness exhibits lower values of components II and III than the 64-Gaussian case, making it the most effective configuration to promote turbulence isotropy.

### 3.5. Analysis of turbulent structures and rough wall effects

In this study, the effects of irregular rough walls on turbulence are explored through the analysis of turbulence structures, specifically streaks and vortical formations. Streaks, as defined by Hutchins et al. (2012), can have context-dependent interpretations. In this research, streaks refer to coherent structures of slow-moving fluid, predominantly found in near-wall regions, identified through streamwise velocity fluctuations. Consistent with the observations of Hutchins and Marusic (2007), these streaks are characterized as Low- and High-Momentum Regions (LMRs and HMRs), with low-speed regions flanked by high-speed regions. In smooth-wall layers, streaks typically exhibit a streamwise-elongated shape (De Marchis et al., 2010). However, wall roughness selectively alters this coherent pattern, with the roughness shape and density influencing the distribution and behavior of turbulent structures. To explore this, the study employs contour plots and 3D iso-surfaces to identify streaks, using the ratio between velocity fluctuations and their root mean square values. For each roughness level, turbulent structures are analyzed on horizontal planes, with characteristics evolving as the distance from the wall increases. This plane-based analysis allows for a comparison between turbulent structures in smooth and rough-wall cases. In Fig. 9 turbulent structures on a horizontal plane for both smooth and rough walls are illustrated. Specifically, left panels are referred to the 32-Gaussian roughness, whereas right panels report the streak structures of 64-Gaussian roughness. The roughness increase from the upper to the lower tails. Previous studies, which analyzed the root mean square values of streamwise velocity

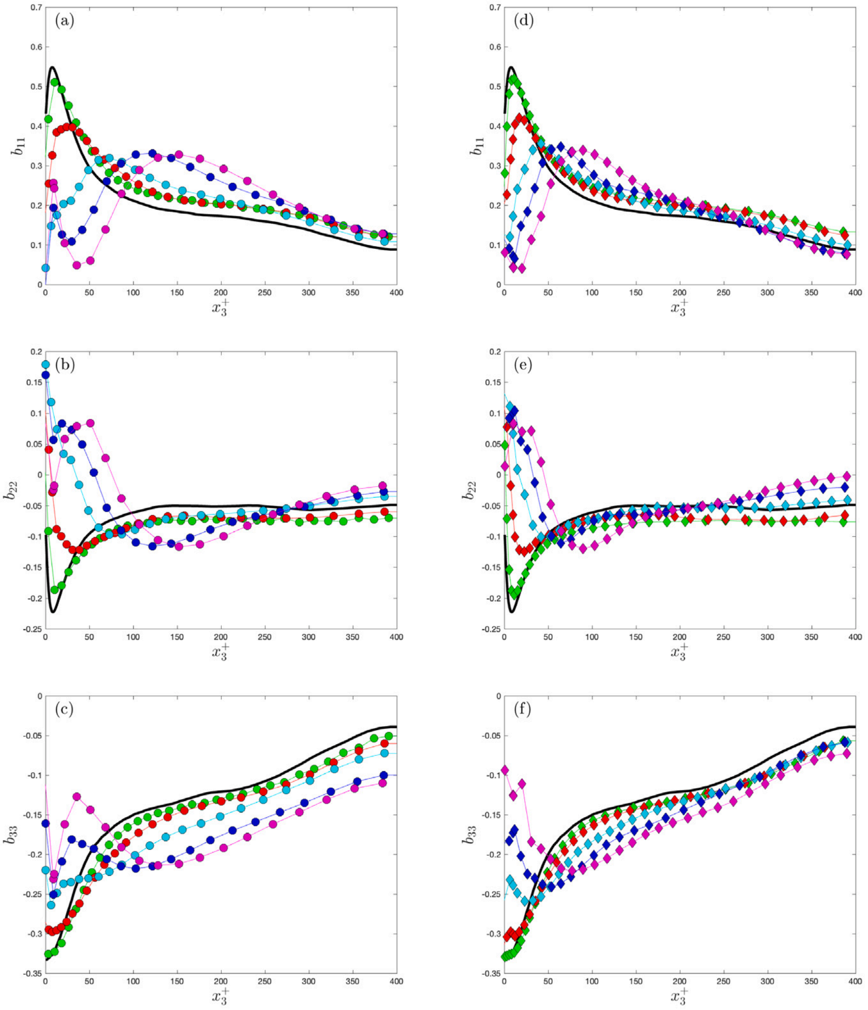

**Fig. 7.** Components of the Reynolds stress anisotropy tensor for the cases studied. $b_{11}$: (a) 32, (b) 64; $b_{22}$: (c) 32, (d) 64; $b_{33}$: (e) 32, (f) 64. Colors and symbols correspond to those in Table 1.

fluctuations and amplitude modulation (AIM), have shown that the distance from the wall at which turbulent structures reach maximum anisotropy increases with roughness. For the smooth-wall case (Fig. 9a), this distance is approximately $x_3^+ \approx 10$. In contrast, for rough-wall cases, this distance ranges from $18 < x_3^+ < 152$, depending on the roughness level. Despite relatively small roughness heights (e.g., $\overline{k} = 0.005 \cdot h$, shown in Figs. 9b-c), roughness near the wall causes a noticeable reduction in the longitudinal elongation of streaks. As the roughness height increases, the distance from the wall at which streaks achieve maximum elongation also increases. Additionally, these streaks exhibit intermittent behavior driven by wall-induced fluctuations, underscoring the influence of roughness on the coherent pattern of streaks. The analysis of turbulent structures further corroborates findings from velocity profile evaluations and turbulent intensity investigations, highlighting the role of roughness in altering the spatial characteristics and dynamics of turbulence near the wall. Comparing the contour plots depicted in the left panels of Fig. 9 and those reported in the right panels, it can be argue, once again, how 32-Gaussian roughness causes higher effect than 64-Gaussian shape. It is evident, keeping constant the roughness height, a reduction of elongated structures in the streamwise direction and a streak enlargement in the spanwise direction. Moreover the height at which the streaks achieve a maximum elongation is systematically higher for 32-Gaussian functions. The roughness effect can also be observed in apparent smearing of the streaky structures depicted in Fig. 9. This behavior is given by two main reasons. The primary is given by the effect of the roughness below the plotted slices. The roughness peaks are, in fact, higher than the mean roughness height causing local disruption of the coherent structure in presence of the roughness pinnacles. Furthermore, the 2D nature of the roughness enhance this typical behavior, less evident in 3D rough walls, as already observed by De Marchis et al. (2015).

The qualitative results are in perfect agreement with the quantitative analyses given by the anisotropy tensor and confirm the tendency towards isotropization highlighted through the AIM analysis. Despite the huge differences induced by the roughness, a somewhat of alternating positive and negative pattern behavior is persistent also for the highest roughness simulated. Clearly the number of alternating structures in the spanwise direction is dramatically reduced due to their increase in dimension in the same direction. Connected with the coherent streaky structures are the vortical structures of the rotating vortex. In order to further investigate on the effect of the roughness on turbulence, vortical structures are thus investigated through 3D visualization.

Fig. 10 presents 3D iso-surfaces of wall-normal vorticity $\omega_{x_3}$. For each depicted case, the plotted iso-surfaces correspond to a value of $\omega_{x_3} \approx \pm 0.20 |\omega_{x_3}|_{\max}$. For clarity, the contour of the roughness height is superimposed on the vortical structures. The red regions indicate roughness peaks, while the blue zones correspond to cavity regions. For small roughness heights ($\overline{k} = 0.005 \cdot h$, Figs. 10a-b), the vortical structures exhibit characteristics typical of smooth-wall behavior. Specifically, the vortices are elongated in the streamwise direction and alternate between positive and negative values. However,

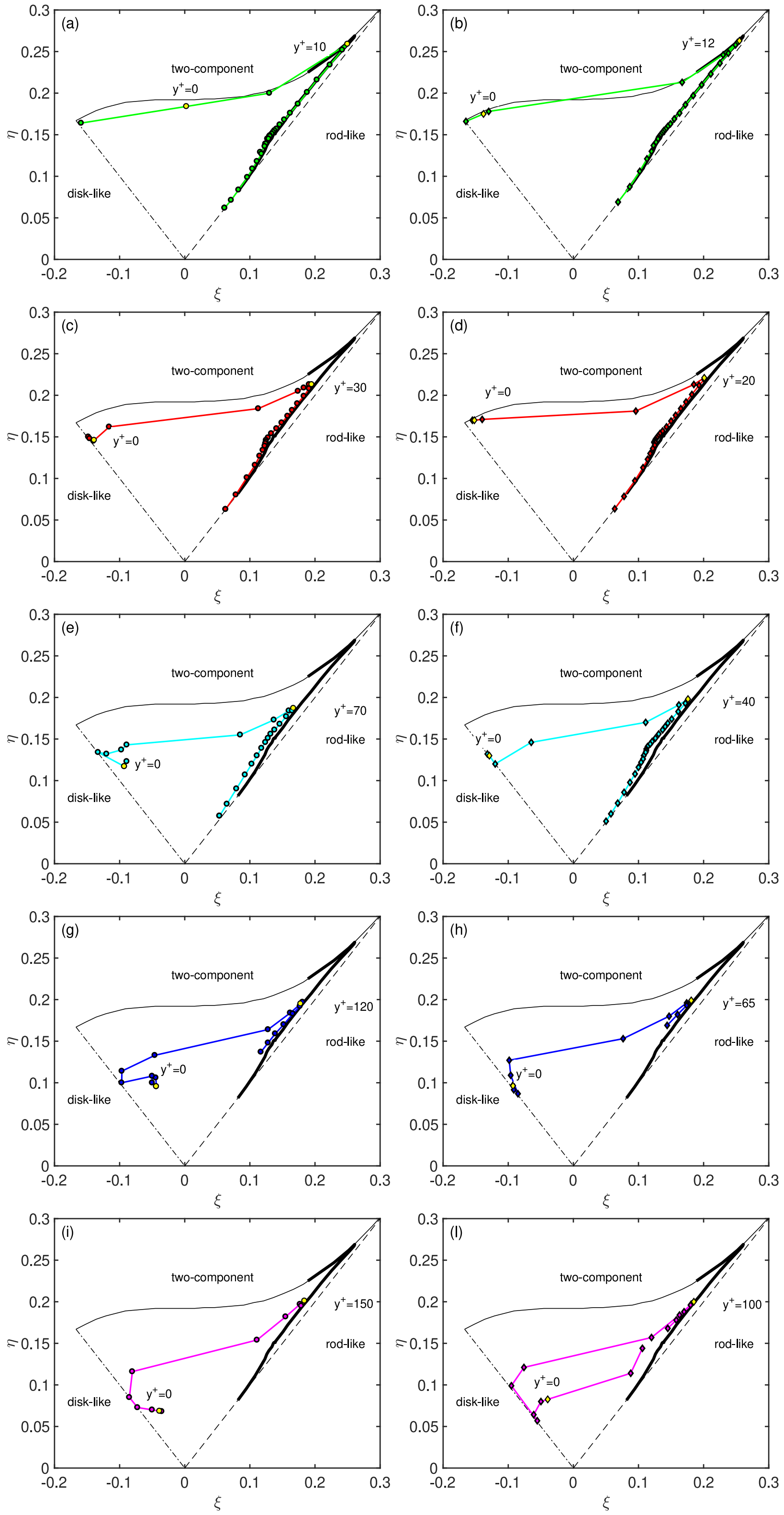

**Fig. 8.** Anisotropy invariant maps (AIM) for rough surfaces, with the smooth-wall case shown for reference. Yellow markers indicate $y^+ = 0$ and the location of maximum streak elongation. Trajectories illustrate the evolution of turbulence anisotropy with increasing distance from the wall and roughness height. (a) 32_0.5; (b) 64_0.5; (c) 32_1; (d) 64_1; (e) 32_2; (f) 64_2; (g) 32_3; (h) 64_3; (i) 32_4; (l) 64_4.

as the roughness height increases, significant alterations occur in both the streamwise and spanwise directions. Increasing roughness height results in a narrowing of streamwise elongation and a widening of the vortical structures in the spanwise direction. Additionally, the inclination of the vortical structures grows in both spanwise and wall-normal directions. The 3D visualization highlights that the effects of

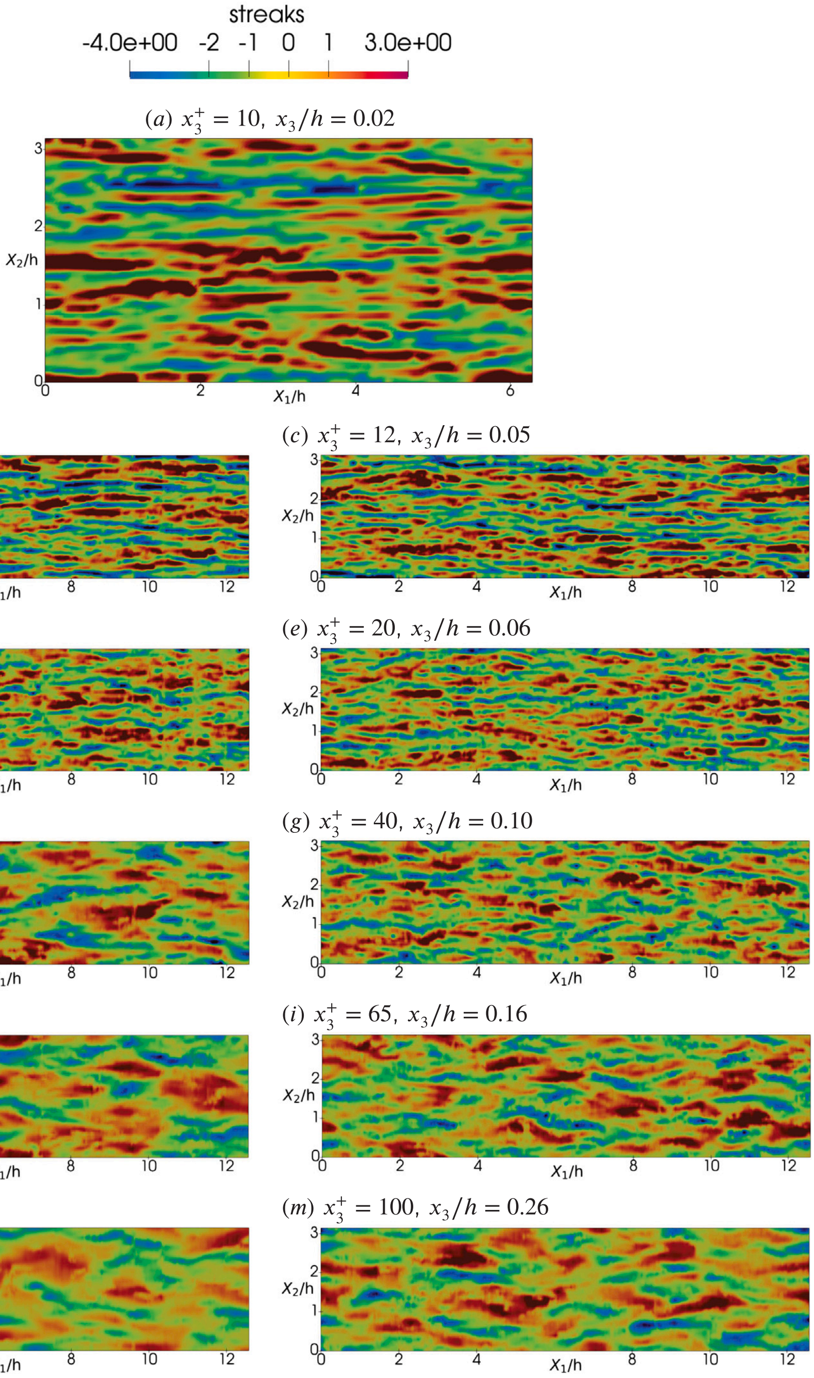

$(a)\ x_3^+ = 10,\ x_3/h = 0.02$

$(b)\ x_3^+ = 20,\ x_3/h = 0.05$

$(c)\ x_3^+ = 12,\ x_3/h = 0.05$

$(d)\ x_3^+ = 30,\ x_3/h = 0.06$

$(e)\ x_3^+ = 20,\ x_3/h = 0.06$

$(f)\ x_3^+ = 70,\ x_3/h = 0.18$

$(g)\ x_3^+ = 40,\ x_3/h = 0.10$

$(h)\ x_3^+ = 120,\ x_3/h = 0.31$

$(i)\ x_3^+ = 65,\ x_3/h = 0.16$

$(l)\ x_3^+ = 150,\ x_3/h = 0.38$

$(m)\ x_3^+ = 100,\ x_3/h = 0.26$

**Fig. 9.** Contour plot of $u_1'/\sqrt{(u_1' \cdot u_1')_t}$ for the cases of study: (a) smooth case; (b) 32_0.5; (c) 64_0.5; (d) 32_1; (e) 64_1; (f) 32_2; (g) 64_2; (h) 32_3; (i) 64_3; (l) 32_4; (m) 64_4.

roughness depend on the type of rough surface. More specifically, the 64-Gaussian roughness causes fewer disruptions to the flow compared to the 32-Gaussian roughness. In the right panels, regions within the flow populated by coherent zones are more elongated than the turbulent structures depicted in the left panels for the 32-Gaussian roughness. Moreover, the 64-Gaussian rough walls lead to a more pronounced development of vortices in both the streamwise and spanwise directions, a trend less evident for the 32-Gaussian rough surfaces. The influence of the roughness density on the vorticity field aligns with the findings of Leonardi et al. (2004), who demonstrated that square-bar roughness introduces significant modifications. For $w/k = 1$, the vorticity contours remain parallel to the plane of the crests and exhibit behavior similar to smooth walls, except for shorter streamwise elongation. At $w/k = 7$, the vorticity field becomes more complex due to the "splashing" effect at the leading edge of the roughness elements. This effect lifts the structures and increases their spanwise width, consistent with the DNS study by Ikeda and Durbin (2007), which observed that transversely mounted rib roughness disrupts the streamwise vortical streaks typical of smooth walls, producing irregular, three-dimensional, incoherent vorticity patterns downstream of the ribs. The above analysis aligns with the quantitative findings, confirming that the 32-Gaussian roughness, due to its wider cavity regions, more effectively disrupts coherent motion than the 64-Gaussian roughness. Following the analysis by Leonardi et al. (2007), it can be concluded that the

[h!]

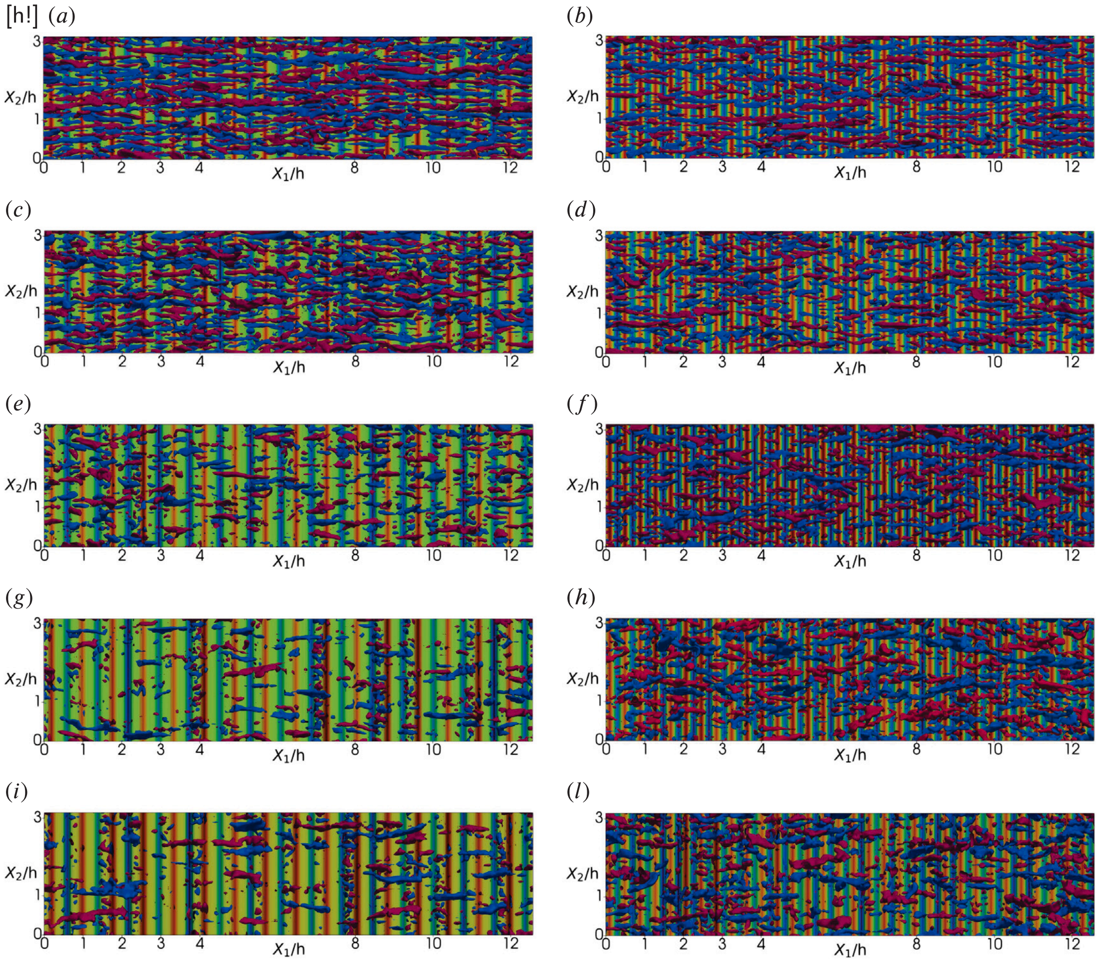

**Fig. 10.** 3D iso-surfaces of wall-normal vorticity $\omega_{x_3}$. For each depicted case the plotted iso-surface correspond to a value of $\omega_{x_3} \approx \pm 0.20|\omega_{x_3}|_{max}$ for 32-Gaussian roughness and a $\omega_{x_3} \approx \pm 0.25|\omega_{x_3}|_{max}$ for 64-Gaussian roughness . Red color indicates roughness peaks, whereas blue zone corresponds to the cavity regions. The contour plot of the roughness height is superimposed to the vortical structure: blue negative values, red positive values. (a) 32_0.5; (b) 64_0.5; (c) 32_1; (d) 64_1; (e) 32_2; (f) 64_2; (g) 32_3; (h) 64_3; (i) 32_4; (l) 64_4. (For interpretation of the references to color in this figure legend, the reader is referred to the web version of this article.)

32-Gaussian roughness behaves like the k-type roughness, whereas the 64-Gaussian roughness behaves like the d-type roughness.

To give more insight on the effect of the roughness on vortical structures, Fig. 11 highlights that, with 64-Gaussian roughness and $\overline{k} = 0.005 \cdot h$, the structures remain elongated in the flow direction without significant upward inclination. In contrast, with the 32-Gaussian roughness at $\overline{k} = 0.005 \cdot h$, there is a noticeable increase in upward inclination and the structures appear shorter. For 64-Gaussian roughness with $\overline{k} = 0.04 \cdot h$, while the structures are inclined upward and exhibit significant broadening, appearing almost spherical, they maintain an alternation in the $x_2$ and elongation in the $x_1$ directions. In the case of 32-Gaussian roughness with $\overline{k} = 0.04 \cdot h$, the structures are almost completely fragmented into numerous smaller, more spherical structures rather than elongated ones.

In order to discuss in a more quantitative way the results on the coherent structures above reported, the two-point spatial correlations of the streamwise (Figs. 12(a)–(b)) and wall-normal (Figs. 12(c)–(d)) velocity fluctuations are plotted along both the streamwise and spanwise directions at a wall-normal distance of $x_3^+ = 20$. Roughness reduces correlations in the streamwise direction while enhancing them in the spanwise direction, indicating that turbulent structures become shorter in the streamwise direction and wider in the spanwise direction as roughness increases, consistent with the observations in Figs. 9 and 10. The general behavior is consistent with previous literature findings over 3D roughness shapes (see, Bhaganagar et al., 2004) and over a pseudo-roughness analysis where the roughness is parameterized using 2D shape functions (see, Busse and Sandham, 2012). In Fig. 12a, cases with $k/h = 0.005$ (● 32_0.5, ◆ 64_0.5) retain higher levels of correlation than cases with $k/h = 0.3$ (● 32_3, ◆ 64_3) where the correlation decays more rapidly. For $k/h = 0.005$, the differences between the 32-Gaussian and 64-Gaussian configurations are negligible, whereas at $k/h = 0.03$ a slight divergence appears, with the 32-Gaussian case exhibiting lower correlations. In Fig. 12b, consistent with Leonardi et al. (2003), the reduction in the minimum values of the spanwise correlation highlights the weakening of the alternating positive–negative pattern that is characteristic of smooth-wall turbulence. Notably, cases with $k/h = 0.005$ display more elongated turbulent structures compared to those at $k/h = 0.03$. As also noted by Bhaganagar et al. (2004), two-point correlations of the wall-normal velocity provide an alternative means to estimate the deflection of vortical streaks. Figs. 12c–d show that, at $x_3^+ = 20$, the average streamwise extent of the near-wall vortices is reduced with increasing roughness, while their average spanwise diameter increases. Substantially, qualitative and quantitative results demonstrate that roughness causes a decrease of the streamwise coherent length and an increase of the spanwise turbulent structure dimension.

## 4. Conclusions

This study advances the understanding of turbulence dynamics over irregular rough surfaces by extending the work of Bruno et al. (2024b),

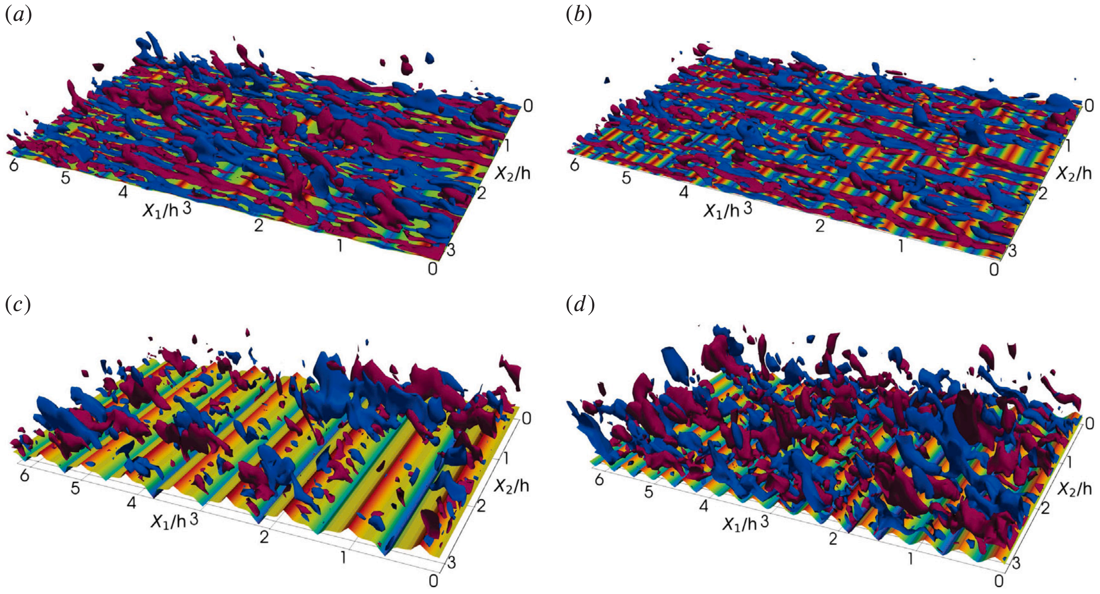

**Fig. 11.** 3D iso-surfaces of wall-normal vorticity $\omega_{x_3}$. Red color indicates roughness peaks, whereas blue zone corresponds to the cavity regions. The contour plot of the roughness height is superimposed to the vortical structure: blue negative values, red positive values. (a) 32_0.5; (b) 64_0.5; (c) 32_4; (d) 64_4. (For interpretation of the references to color in this figure legend, the reader is referred to the web version of this article.)

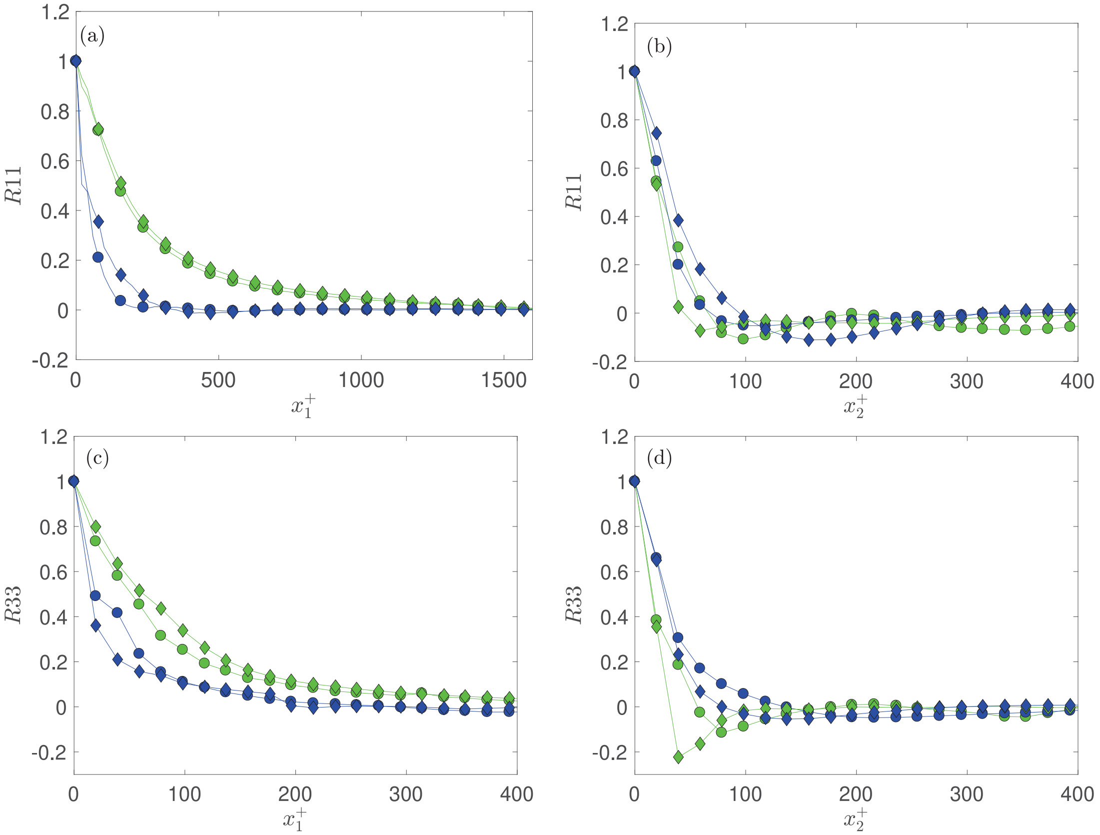

**Fig. 12.** Two-point spatial correlations at $x_3^+ = 20$. (a)–(c) Two-point correlation $R_{11}$ and $R_{33}$ in the streamwise direction. (b)–(d) Two-point correlation $R_{11}$ and $R_{33}$ in the spanwise direction. Symbols: ● 32_0.5, ● 32_3, ◆ 64_0.5, ◆ 64_3. (For interpretation of the references to color in this figure legend, the reader is referred to the web version of this article.)

with a specific focus on the influence of roughness density. Large Eddy Simulations (LES) were employed to simulate turbulent flows over rough walls modeled using Gaussian functions, allowing for an in-depth exploration of the effects of surface roughness on various turbulent quantities. By examining both the height and density of roughness elements, the study provides valuable insights into how these parameters affect the mean velocity profile, turbulence intensity, Reynolds stresses and flow structures. The results confirm that surface roughness significantly affects the mean velocity profile, shifting it downward relative to smooth-wall conditions. This downward shift is proportional to the roughness height, becoming more pronounced as roughness increases. Specifically, increasing the roughness height from $\overline{k} = 0.005 \cdot h$ to $\overline{k} = 0.04 \cdot h$ results in a larger roughness function. Interestingly, the velocity profiles in the outer region does not collapse across all roughness heights, indicating that the outer flow region is partially sensitive to roughness, even though the highest modification are confined in the inner region. The analysis of the root mean square (rms) of velocity fluctuations reveals key trends in turbulence intensity. In the inner layer, velocity fluctuations generally increase as roughness height increases, indicating stronger turbulence near the wall. However, in the outer layer, both turbulence intensity and anisotropy decrease, suggesting a trend towards more isotropic turbulence. This redistribution of turbulence energy from the streamwise direction to the wall-normal and spanwise directions points to more isotropic turbulence near the wall, especially for rough surfaces with lower roughness densities, such as the 32-Gaussian roughness configuration. Further analysis of the turbulent shear stress profiles reveals that increasing roughness height leads to a significant reduction in viscous stress, with Reynolds shear stress dominating the total stress. The density of roughness elements plays a crucial role in the distribution of shear stress. For instance, the 32-Gaussian roughness elements exhibit higher turbulent shear stress compared to the 64-Gaussian configuration at the same roughness height. This suggests that lower-density roughness elements contribute more significantly to turbulence generation, which could be important in practical applications where roughness density is a key design parameter. The study also examines turbulent structures such as streaks and vortices. Wall roughness alters the shape, distribution and dynamics of these coherent turbulent structures. Streaks, identified as Low- and High-Momentum Regions (LMRs and HMRs), exhibit reduced streamwise elongation as the roughness height increases. This change is accompanied by an increase in the distance from the wall at which streaks reach their maximum elongation. As roughness height increases, the flow becomes more intermittent, with stronger wall-induced fluctuations, disrupting the smooth-wall streak pattern. Increased roughness density exacerbates these effects, with 32-Gaussian roughness causing more significant changes in streak behavior than 64-Gaussian roughness. In the study of vortical structures, increasing roughness height leads to significant changes in vortex shape. Vortices become less elongated in the streamwise direction and more spread out in the spanwise direction. These effects are more pronounced for rough surfaces with fewer elements, as observed with the 32-Gaussian elements. These results are in agreement with previous studies suggesting how, not only the roughness height but, the roughness density affects vortical structure generation mechanism, disrupting streamwise vortex alignment. The use of the Anisotropy Invariant Map (AIM) further confirms the roughness-induced changes in turbulence anisotropy. The results show a transition from a near-rod-like state in the smooth-wall case to a more isotropic turbulence state in rough-wall cases, particularly at higher roughness heights. This behavior is more evident for lower-density roughness configurations, such as the 32-Gaussian roughness, which results in a larger reduction in anisotropy and a more isotropic turbulence structure in the inner region. Overall, this study highlights the significant role of both roughness height and density in shaping the turbulence dynamics of flows over rough surfaces. The findings suggest that both roughness height and density significantly influence the mean velocity profile, turbulence intensities, turbulence anisotropy, turbulent shear stresses and the distribution of turbulent structures.

## CRediT authorship contribution statement

**Federica Bruno:** Writing – review & editing, Writing – original draft, Visualization, Validation, Supervision, Software, Resources, Project administration, Methodology, Investigation, Funding acquisition, Formal analysis, Data curation, Conceptualization. **Enrico Napoli:** Writing – review & editing, Writing – original draft, Visualization, Validation, Supervision, Resources, Methodology, Investigation, Formal analysis, Data curation. **Mauro De Marchis:** Writing – review & editing, Writing – original draft, Visualization, Validation, Supervision, Methodology, Investigation, Data curation.

## Funding information

Not funded.

## Declaration of competing interest

The authors declare that they have no known competing financial interests or personal relationships that could have appeared to influence the work reported in this paper.

## Acknowledgments

The authors greatly appreciate the financial support provided by the following projects:

- RETURN Extended Partnership and received funding from the European Union Next-GenerationEU (National Recovery and Resilience Plan – NRRP, Mission 4, Component 2, Investment 1.3 – D.D. 1243 2/8/2022, E0000005);
- TiSento - SENSORIALIZED COMPOSITE PIPE FOR HYDRAULIC APPLICATIONS, n. 084221000550 CUP G18I18001710007. Funded under measure 1.1.5 of the PO FESR SICILY 2014–2020;
- European Union - NextGenerationEU - National Sustainable Mobility Center CN00000023, Italian Ministry of University and Research Decree n. 1033— 17/06/2022, Spoke 3, CUP B73C22000760001

## Data availability

The data that support the findings of this study are available from the corresponding author upon reasonable request.

## References

Abdelaziz, M., Djenidi, L., Ghayesh, M.H., Chin, R., 2022. A new equivalent sand grain roughness relation for two-dimensional rough wall turbulent boundary layers. J. Fluid Mech. 940, 1–23. http://dx.doi.org/10.1017/jfm.2022.242.

Aghaei-Jouybari, M., Yuan, J., Li, Z., Brereton, G.J., Jaberi, F.A., 2023. Supersonic turbulent flows over sinusoidal rough walls. J. Fluid Mech. 956, A3.

Antonia, R.A., Krogstad, P.-A., 2001. Turbulence structure in boundary layers over different types of surface roughness. Fluid Dyn. Res. 28, 139–157. http://dx.doi.org/10.1016/S0169-5983(00)00025-3.

Ashrafian, A., Andersson, H.I., 2006. The structure of turbulence in a rod-roughened channel. Int. J. Heat Fluid Flow 27 (1), 65–79.

Ashrafian, A., Andersson, H.I., Manhart, M., 2004. DNS of turbulent flow in a rod-roughened channel. Int. J. Heat Fluid Flow 25 (3), 373–383. http://dx.doi.org/10.1016/j.ijheatfluidflow.2004.02.004.

Bhaganagar, K., Kim, J., Coleman, G., 2004. Effect of roughness on wall-bounded turbulence. Flow, Turbul. Combust. 72, 463–492. http://dx.doi.org/10.1023/B:APPL.0000044407.34121.64.

Bruno, F., De Marchis, M., Leonardi, S., 2024a. Towards a new roughness parametrization through the effective distribution function. J. Fluid Mech. 2024;999:A26, 8–12. http://dx.doi.org/10.1017/jfm.2024.970.

Bruno, F., De Marchis, M., Leonardi, S., 2026. Direct numerical simulations of turbulent channel flow roughened with 2D triangular bars: On the effective distribution parametrization. Int. J. Heat Fluid Flow 117, 110015.

Bruno, F., De Marchis, M., Napoli, E., 2024b. The role of the areal parameters on turbulent flow over 2D Gaussian roughness. Int. J. Heat Fluid Flow 106, 109287.

Busse, A., Jelly, T.O., 2020. Influence of surface anisotropy on turbulent flow over irregular roughness. Flow, Turbul. Combust. 104, 331–354.

Busse, A., Sandham, N.D., 2012. Parametric forcing approach to rough-wall turbulent channel flow. J. Fluid Mech. 712, 169–202.

Celik, I.B., Cehreli, Z.N., Yavuz, I., 2005. Index of resolution quality for large eddy simulations. J. Fluids Eng. 127, 949–958.

Choi, H., Moin, P., 2012. Grid-point requirements for large eddy simulation: Chapman's estimates revisited. Phys. Fluids 24 (1).

Chung, D., Hutchins, N., Schultz, M.P., Flack, K.A., 2021. Predicting the drag of rough surfaces. Annu. Rev. Fluid Mech. 53 (1), 439–471.

Coceal, O., Thomas, T.G., Castro, I.P., Belcher, S.E., 2006. Mean flow and turbulence statistics over groups of urban-like cubical obstacles. Bound.-Layer Meteorol. 121, 491–519.

Colebrook, C.F., Blench, T., Chatley, H., Essex, E., Finniecome, J., Lacey, G., Williamson, J., Macdonald, G., 1939. Correspondence. turbulent flow in pipes, with particular reference to the transition region between the smooth and rough pipe laws. J. Inst. Civ. Eng. 12 (8), 393–422.

De Maio, M., Latini, B., Nasuti, F., Pirozzoli, S., 2023. Direct numerical simulation of turbulent flow in pipes with realistic large roughness at the wall. J. Fluid Mech. 974, 1–25. http://dx.doi.org/10.1017/jfm.2023.728.

De Marchis, M., 2016. Large eddy simulations of roughened channel flows: Estimation of the energy losses using the slope of the roughness. Comput. Fluids 140, 148–157. http://dx.doi.org/10.1016/j.compfluid.2016.09.021.

De Marchis, M., Milici, B., Napoli, E., 2015. Numerical observations of turbulence structure modification in channel flow over 2D and 3D rough walls. Int. J. Heat Fluid Flow 56, 108–123. http://dx.doi.org/10.1016/j.ijheatfluidflow.2015.07.002.

De Marchis, M., Milici, B., Napoli, E., 2019. Large eddy simulations on the effect of the irregular roughness shape on turbulent channel flows. Int. J. Heat Fluid Flow 80, 108494. http://dx.doi.org/10.1016/j.ijheatfluidflow.2019.108494.

De Marchis, M., Napoli, E., 2012. Effects of irregular two-dimensional and three-dimensional surface roughness in turbulent channel flows. Int. J. Heat Fluid Flow 36, 7–17.

De Marchis, M., Napoli, E., Armenio, V., 2010. Turbulence structures over irregular rough surfaces. J. Turbul. 11, 1–32. http://dx.doi.org/10.1080/14685241003657270.

De Marchis, M., Saccone, D., Milici, B., Napoli, E., 2020. Large eddy simulations of rough turbulent channel flows bounded by irregular roughness: Advances toward a universal roughness correlation. Flow, Turbul. Combust. 105, 627–648. http://dx.doi.org/10.1007/s10494-020-00167-5.

Dirling, J., 1973. A method for computing roughwall heat transfer rates on reentry nosetips. In: 8th Thermophysics Conference. p. 763.

Djenidi, L., Elavarasan, R., Antonia, R.A., 1999. The turbulent boundary layer over transverse square cavities. J. Fluid Mech. 395, 271–294.

Flack, K.A., Schultz, M.P., 2014. Roughness effects on wall-bounded turbulent flows. Phys. Fluids 26 (10).

Flack, K.A., Schultz, M.P., Volino, R.J., 2020. The effect of a systematic change in surface roughness skewness on turbulence and drag. Int. J. Heat Fluid Flow 85, 108669.

Ganju, S., Bailey, S.C.C., Brehm, C., 2022. Amplitude and wavelength scaling of sinusoidal roughness effects in turbulent channel flow at fixed. J. Fluid Mech. 937, http://dx.doi.org/10.1017/jfm.2022.118.

Garg, H., Wang, L., Sahut, G., Fureby, C., 2023. Large eddy simulations of fully developed turbulent flows over additively manufactured rough surfaces. Phys. Fluids 35 (4), 1–20. http://dx.doi.org/10.1063/5.0143863, arXiv:2302.00631.

Hama, F.R., 1954. Boundary layer characteristics for smooth and rough surfaces. In: Society of Naval Architects and Marine Engineers.

Hutchins, N., Chauhan, K., Marusic, I., Monty, J., Klewicki, J., 2012. Towards reconciling the large-scale structure of turbulent boundary layers in the atmosphere and laboratory. Bound.-Layer Meteorol. 145 (2), 273–306.

Hutchins, N., Marusic, I., 2007. Evidence of very long meandering features in the logarithmic region of turbulent boundary layers. J. Fluid Mech. 579, 1–28.

Ikeda, T., Durbin, P.A., 2007. Direct simulations of a rough-wall channel flow. J. Fluid Mech. 571, 235–263.

Jalalabadi, R., Stoesser, T., 2022. Reynolds and dispersive shear stress in free-surface turbulent channel flow over square bars. Phys. Rev. E 105 (3), 1–10. http://dx.doi.org/10.1103/physreve.105.035102.

Kaminaris, I., Balaras, E., Vishwanathan, V., Schultz, M.P., 2026. On the impact of frontal solidity on turbulent boundary layers over irregular bio-inspired surfaces. Int. J. Heat Fluid Flow 117, 109991.

Kim, J., Moin, P., Moser, R., 1987. Turbulence statistics in fully developed channel flow at low Reynolds number. J. Fluid Mech. 177, 133–166.

Kuwata, Y., Yagasaki, W., Suga, K., 2024. Effects of steepness on turbulent heat transfer over sinusoidal rough surfaces. Int. J. Heat Fluid Flow 109 (July), 109537. http://dx.doi.org/10.1016/j.ijheatfluidflow.2024.109537.

Lee, J.H., Sung, H.J., Krogstad, P.-Å., 2011. Direct numerical simulation of the turbulent boundary layer over a cube-roughened wall. J. Fluid Mech. 669, 397–431.

Leonardi, S., Orlandi, P., Antonia, R.A., 2007. Properties of d- and k-type roughness in a turbulent channel flow. Phys. Fluids 19 (12).

Leonardi, S., Orlandi, P., Djenidi, L., Antonia, R.A., 2004. Structure of turbulent channel flow with square bars on one wall. Int. J. Heat Fluid Flow 25 (3), 384–392.

Leonardi, S., Orlandi, P., Djenidi, L., Antonia, R.A., 2006. Guidelines for modeling a 2D rough wall channel flow. Flow, Turbul. Combust. 77 (1–4), 41–57.

Leonardi, S., Orlandi, P., Smalley, R.J., Djenidi, L., Antonia, R.A., 2003. Direct numerical simulations of turbulent channel flow with transverse square bars on one wall. J. Fluid Mech. 491, 229–238.

Lumley, J.L., 1979. Computational modeling of turbulent flows. Adv. Appl. Mech. 18, 123–176.

Ma, G.-Z., Xu, C.-X., Sung, H.J., Huang, W.-X., 2022. Scaling of rough-wall turbulence in a transitionally rough regime. Phys. Fluids 34 (3), 031701. http://dx.doi.org/10.1063/5.0084646.

Maaß, C., Schumann, U., 1996. Direct numerical simulation of separated turbulent flow over a wavy boundary. In: Flow Simulation with High-Performance Computers II: DFG Priority Research Programme Results 1993–1995. Springer, pp. 227–241.

Mazouz, N., Flätgen, G., Krischer, K., Kevrekidis, I.G., 1998. The impact of the operation mode on pattern formation in electrode reactions: From potentiostatic to galvanostatic control. J. Electrochem. Soc. 145 (7), 2404.

Meneveau, C., 1994. Statistics of turbulence subgrid-scale stresses: Necessary conditions and experimental tests. Phys. Fluids 6 (2), 815–833.

Milici, B., De Marchis, M., 2016. Statistics of inertial particle deviation from fluid particle trajectories in horizontal rough wall turbulent channel flow. Int. J. Heat Fluid Flow 60, 1–11. http://dx.doi.org/10.1016/j.ijheatfluidflow.2016.03.008.

Miyake, Y., Tsujimoto, K., Nagai, N., 2002. Numerical simulation of channel flow with a rib-roughened wall. J. Turbul. 3 (1), 035.

Moody, L.F., 1944. Friction factors for pipe flow. Trans. Asme 66, 671–684.

Nair, S.S., Wadhai, V.A., Kunz, R.F., Yang, X.I.A., 2024. Rough surfaces in underexplored surface morphology space and their implications on roughness modelling. J. Fluid Mech. 999, 1–34. http://dx.doi.org/10.1017/jfm.2024.956, arXiv:2409.06089.

Napoli, E., Armenio, V., De Marchis, M., 2008. The effect of the slope of irregularly distributed roughness elements on turbulent wall-bounded flows. J. Fluid Mech. 613, 385–394. http://dx.doi.org/10.1017/S0022112008003571.

Nikuradse, J., 1933. Laws of flow in rough pipes. pp. 1–62, NACA TM 1292 (1950).

Orlandi, P., Leonardi, S., Tuzi, R., Antonia, R., 2003. Direct numerical simulation of turbulent channel flow with wall velocity disturbances. Phys. Fluids 15 (12), 3587–3601.

Piomelli, U., Balaras, E., 2002. Wall-layer models for large-eddy simulations. Annu. Rev. Fluid Mech. 34 (1), 349–374.

Pope, S.B., 2000. Turbulent Flows. Cambridge University Press.

Schlichting, H., 1937. Experimental Investigation of Surface Roughness. Technical Report TM 823, NACA.

Shafi, H.S., Antonia, R.A., 1995. Anisotropy of the Reynolds stresses in a turbulent boundary layer on a rough wall. Exp. Fluids 18 (3), 213–215.

Sigal, A., Danberg, J.E., 1990. New correlation of roughness density effect on the turbulent boundary layer. AIAA J. 28 (3), 554–556. http://dx.doi.org/10.2514/3.10427.

Smalley, R., Leonardi, S., Antonia, R., Djenidi, L., Orlandi, P., 2002. Reynolds stress anisotropy of turbulent rough wall layers. Exp. Fluids 33 (1), 31–37.

Van Rij, J.A., Belnap, B.J., Ligrani, P.M., 2002. Analysis and experiments on three-dimensional, irregular surface roughness. J. Fluids Eng. Trans. ASME 124, 671–677. http://dx.doi.org/10.1115/1.1486222.

Varma, H., Jagadeesan, K., Narasimhamurthy, V.D., Kesarkar, A.P., Andersson, H.I., 2021. LES and DNS of symmetrically roughened turbulent channel flows. Acta Mech. http://dx.doi.org/10.1007/s00707-021-03082-6.

Viggiano, B., Bossuyt, J., Ali, N., Meyers, J., Cal, R.B., 2022. Secondary motions above a staggered multi-scale rough wall. J. Fluid Mech. 2022;941:R1, 1–11. http://dx.doi.org/10.1017/jfm.2022.262.

Vreman, B., Geurts, B., Kuerten, H., 1996. COMPARISION of numerical schemes in large-eddy simulation of the temporal mixing layer. Internat. J. Numer. Methods Fluids 22 (4), 297–311.

Yang, J., Stroh, A., Lee, S., Bagheri, S., Frohnapfel, B., Forooghi, P., 2023. Prediction of equivalent sand-grain size and identification of drag-relevant scales of roughness - a data-driven approach. J. Fluid Mech. 975, 1–24. http://dx.doi.org/10.1017/jfm.2023.881, arXiv:2304.08958.

Zang, Y., Street, R.L., Koseff, J.R., 1993. A dynamic mixed subgrid-scale model and its application to turbulent recirculating flows. Phys. Fluids A: Fluid Dyn. 5 (12), 3186–3196.